electronics

MDPI

Review

A Survey of MMIC Active Filters

Leonardo Pantoli [1,*], Giorgio Leuzzi [1], Francois Deborgies [2], Petar Jankovic [2] and Francesco Vitulli [3]

[1] Department of Industrial and Information Engineering and Economics, University of L'Aquila, 67100 L'Aquila, Italy; giorgio.leuzzi@univaq.it
[2] Directorate of Technology, Engineering and Quality, ESA-ESTEC, 2201 Noordwijk, The Netherlands; Francois.Deborgies@esa.int (F.D.); Petar.Jankovic@esa.int (P.J.)
[3] Thales Alenia Space s.p.a., Via Saccomuro, 00131 Roma, Italy; Francesco.Vitulli@thalesaleniaspace.com
* Correspondence: leonardo.pantoli@univaq.it

Abstract: High-Q filters are a critical component in many systems. However, high-Q filters require very low-loss passive elements that are not compatible with monolithic technology. Therefore, filters are often implemented as off-chip components. Tunable high-Q filters require even larger space and weight, and are usually quite bulky. Active filters have been proposed in the past for a monolithic implementation. However, it is not easy to fulfil such requirements as a high dynamic range, low power consumption, low noise, wide tunability, stability, etc. With this study, we propose a survey of the main solutions presented in the literature, investigating the fulfilment of all or most requirements and their potential applications and feasibility, to be used in practical applications.

Keywords: active filters; filters architecture; integrated filters; MMIC; tunable filters

Citation: Pantoli, L.; Leuzzi, G.; Deborgies, F.; Jankovic, P.; Vitulli, F. A Survey of MMIC Active Filters. *Electronics* **2021**, *10*, 1680. https://doi.org/10.3390/electronics10141680

Academic Editor: Paulo de Souza

Received: 19 May 2021
Accepted: 8 July 2021
Published: 14 July 2021

1. Introduction

Microwave active filters were first proposed fifty years ago, and since then a plurality of approaches have been tried. However, no such device has reached a level of maturity such that a commercial product could be released.

In the following, a review of the main approaches and results available in the literature so far will be presented. A special emphasis will be given to tunable solutions and to proving high-frequency monolithic implementations. As a general remark, results are almost always only promising, but unsatisfactory from the point of view of practical specifications. In almost no case has a suitable effort been devoted to the goal of developing an actual product.

There are three main approaches to the design of microwave active filters: the first is based on the use of components with a negative resistive part, the second is based on the combination of amplifiers and passive filters, while the third is based on the use of switches and capacitors. Components with a negative resistive part (for instance, active inductors) may internally include an amplifier within a feedback loop or may be based on a potentially unstable active device (therefore, on internal feedback). Filters based on the combination of amplifiers and passive networks belong to two main groups: cascaded filters and recursive filters. We will review these different categories separately.

2. Filters Based on the Combination of Amplifiers and Passive Structures

2.1. Cascaded Filters

The basic structure consists of passive filtering structures separated by amplifiers (Figure 1). If the amplifiers are ideal, then the single filtering sections are decoupled and the filtering action is most effective, especially out-of-band. In practice, the amplifiers are matched at 50 Ω, but still provide isolation between the stages.

This approach has no inherent high-frequency or bandwidth limitations. It also has the advantage of a limited noise figure, because the gain of the amplifying stages reduces

the noise contribution of the following sections. Therefore, the filter usually has a positive overall gain. As a drawback, the filter relies only on the passive sections for frequency tuning, typically by means of varactors.

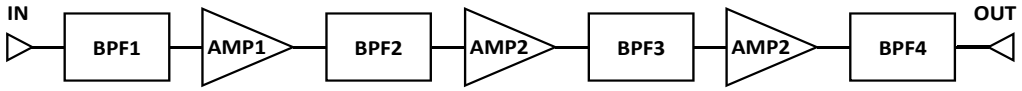

Figure 1. Ideal cascaded filter topology.

Only a few examples have been published, and only two tunable ones. A first example of a fixed-frequency wideband filter from 1982 is shown in Figure 2 (left) [1], where the topology of the individual cells is reported. The full filter is composed of two GaAs chips, each with three passive filtering structures and two feedback amplifiers. The chips are then assembled in a carrier (Figure 2 right). The passband is 5–8 GHz, with a 10 dB gain and better than 10 dB input match (Figure 3). No information is given on the output match, noise figure and compression.

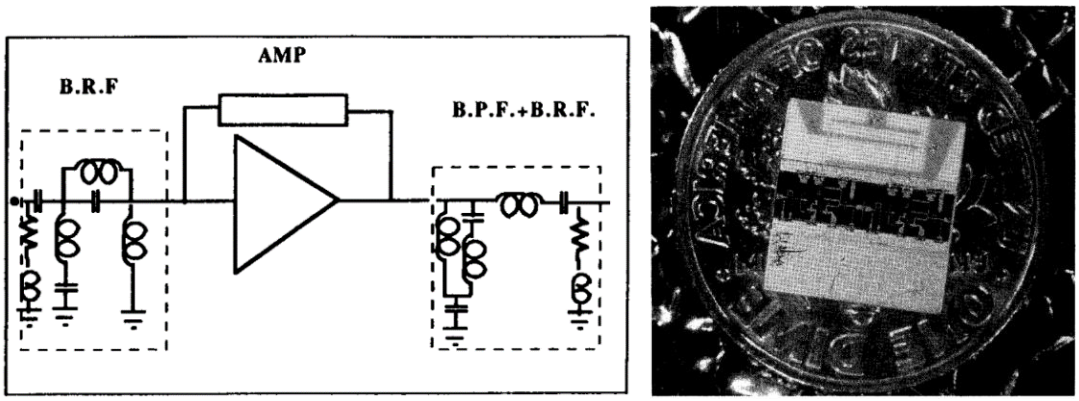

Figure 2. The topology of the individual cell from [1] (**left**) and the complete two-chip filter (**right**). Reproduced with permission from [1].

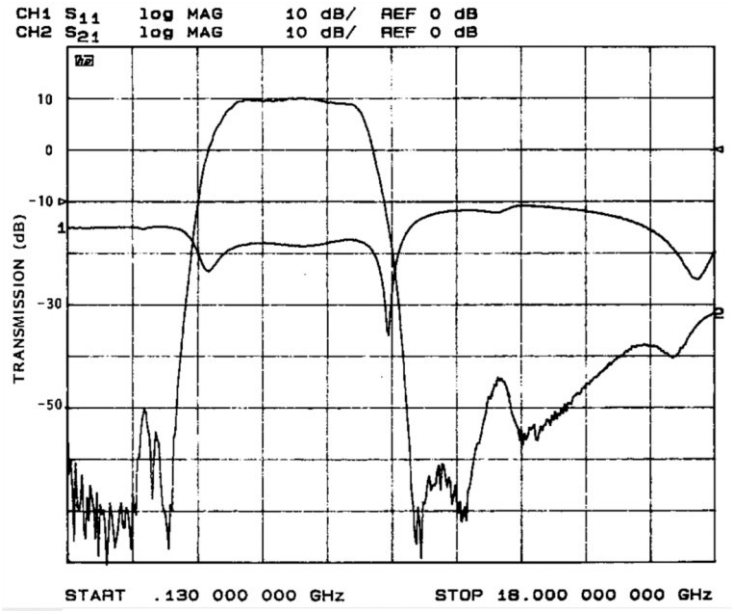

Figure 3. The S-parameters of the filter from [1]. Reproduced with permission from [1].

A similar filter has been published by the same group in [2] in 1990, with similar topology and results, but with a single chip. The noise figure is relatively low, at approximately 4 dB. The measured S-parameters and the noise figure are shown in Figure 4.

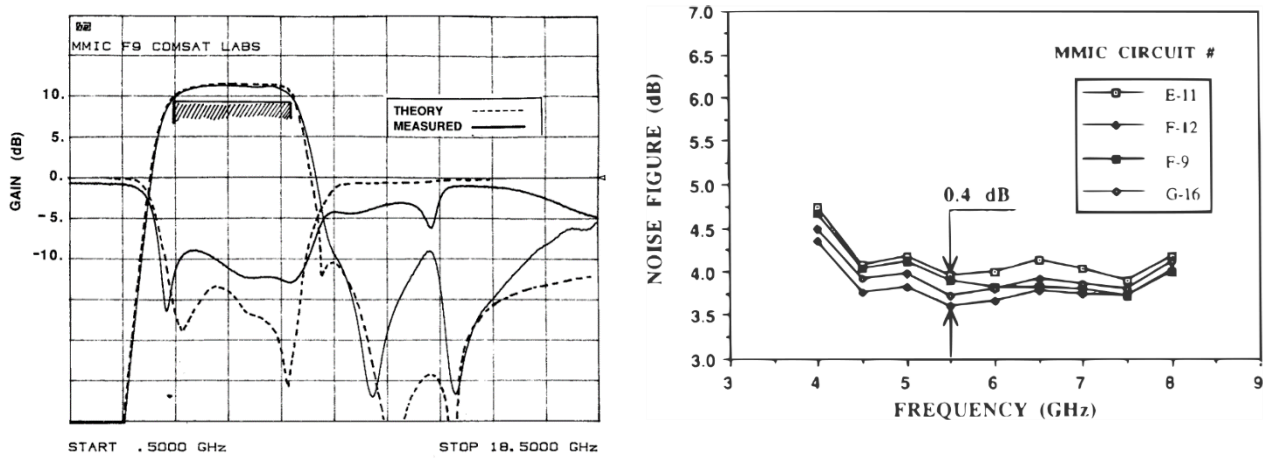

(**a**) (**b**)

Figure 4. The S-parameters (**a**) and the noise figure (**b**) of the filter from [2]. Reproduced with permission from [2].

A second, narrowband example centered at 1.5 GHz has been published in [3]. The schematic is shown in Figure 5, and is based on actively-coupled resonators. The GaAs chip and the measured transfer function are shown in Figure 6. No information is given on the return loss, noise figure or compression.

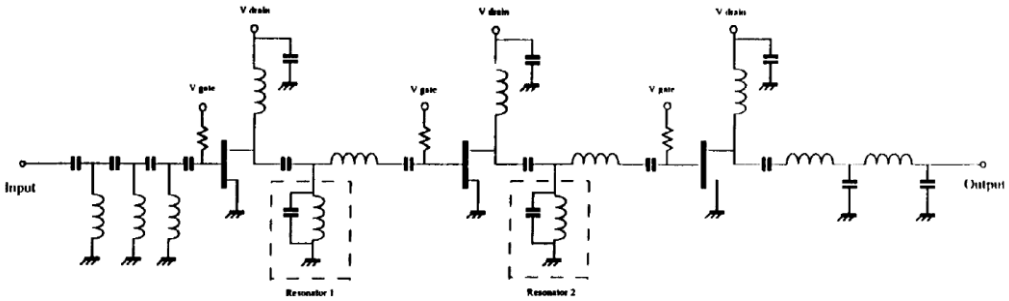

Figure 5. The schematic of the filter from [3]. Reproduced with permission from [3].

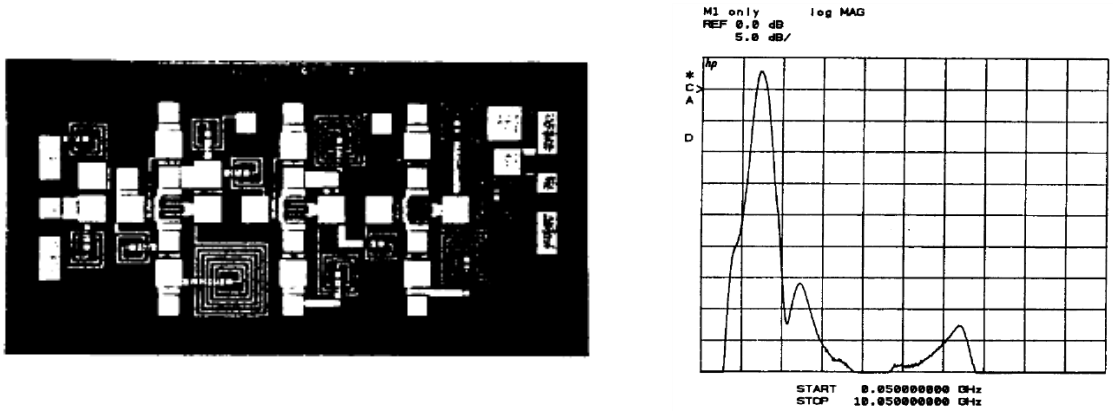

(**a**) (**b**)

Figure 6. The chip photograph (**a**) and the measured transfer function (**b**) of the filter from [3]. Reproduced with permission from [3].

These examples date back to the early 90s, and are implemented in GaAs MESFET technologies. Their frequency is relatively low. The third example of fixed-frequency implementation has been published in 2010 [4] and shows an implementation with BiCMOS technology with 26 GHz center frequency, with comparable results. The passive filtering sections and the gain blocks are implemented on separate chips (Figure 7) and cascaded in the final assembly, including eight gain blocks and three passive filtering sections. The schematics of the active and passive sections are shown in Figure 8.

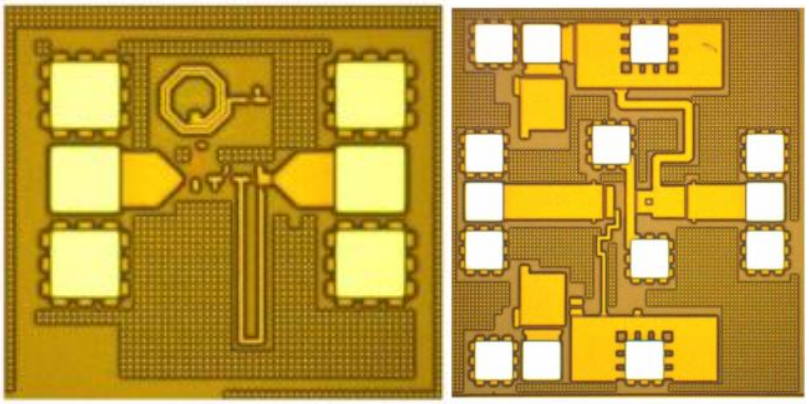

(**a**) (**b**)

Figure 7. The passive filtering chip (**a**) and the active gain block chip (**b**) from [4]. Reproduced with permission from [4].

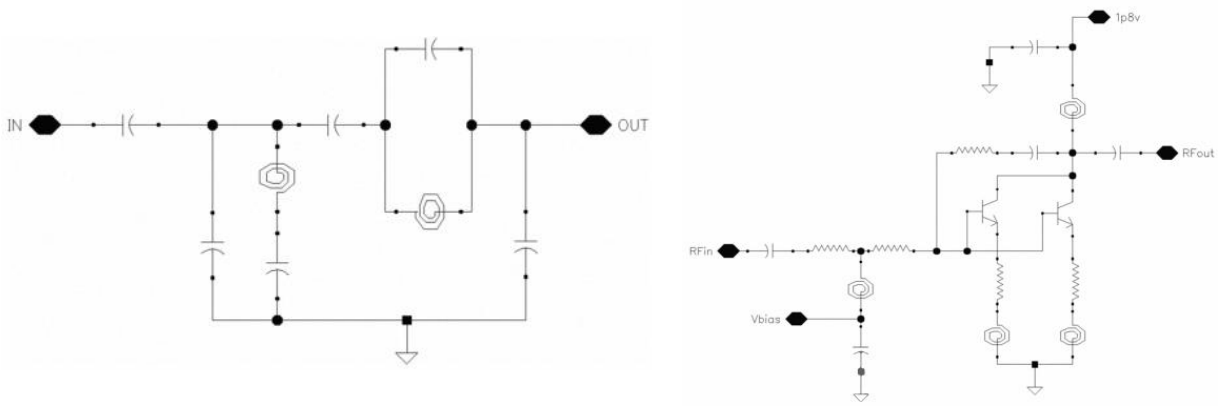

(**a**) (**b**)

Figure 8. The schematic of the passive filtering section (**a**) and of the active gain block (**b**) from [4]. Reproduced with permission from [4].

The simulated and measured S-parameters of both the passive and the gain blocks are shown in Figure 9, and the measured transfer function of the complete cascaded filter is shown in Figure 10a, showing a 25–27 GHz band with excellent selectivity. The simulated and measured two-tone compression and intermodulation curves for the gain block are shown in Figure 10b (with no information on the complete filter), and the simulated noise figure is 5.4 dB.

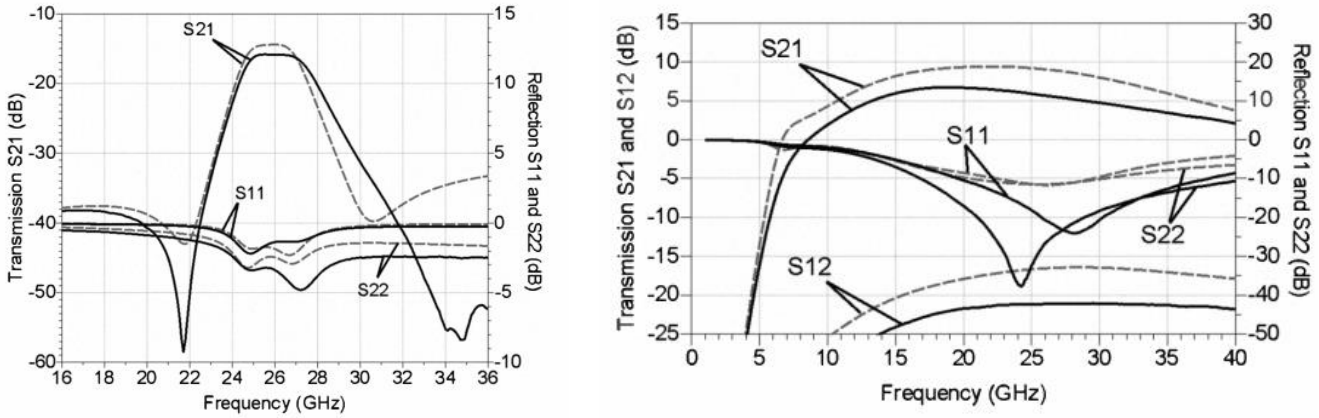

(**a**) (**b**)

Figure 9. The S-parameters of the passive filtering chip (**a**) and of the active gain chip (**b**) from [4]. Simulations are in dashed lines, while measurements in solid lines. Reproduced with permission from [4].

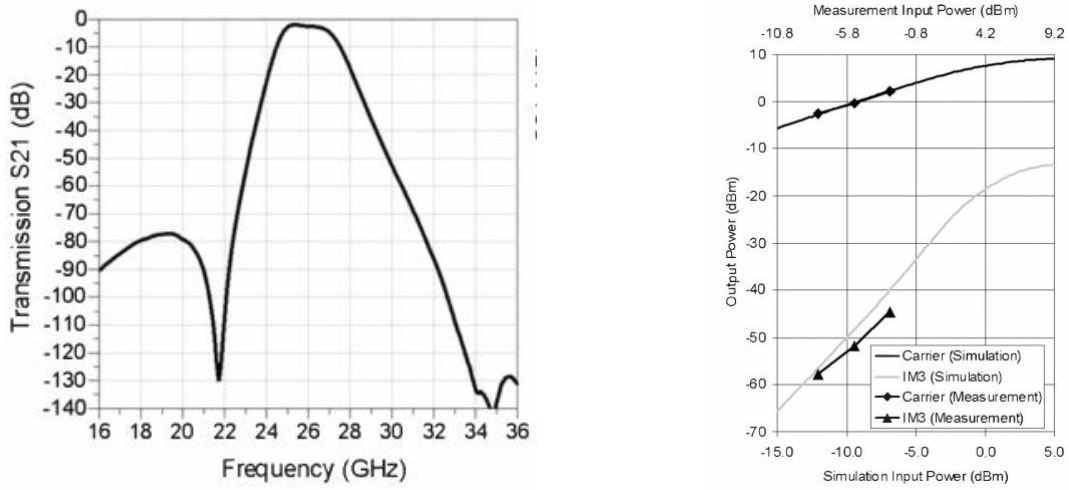

(**a**) (**b**)

Figure 10. The S-parameters of the passive filtering chip (**a**) and of the active gain chip (**b**) from [4]. Reproduced with permission from [4].

Overall, the cascaded approach for fixed-frequency filters shows good performances for both narrowband and wideband filters, with very good selectivity, a reasonable noise figure and presumably a good compression point. Their advantage over passive filters essentially lies in better selectivity.

More interesting are the examples of tunable filters with the same approach. In fact, only two of them have been published, to the best of our knowledge, and only one in monolithic form. The first one [5] is dated to 2010, and is based on the UMS PH25 technology. Both fixed-frequency and tunable versions of the filter have been realized, both with three cascaded cells. The basic cell for the two versions are shown in Figure 11, and their chip implementations are shown in Figure 12.

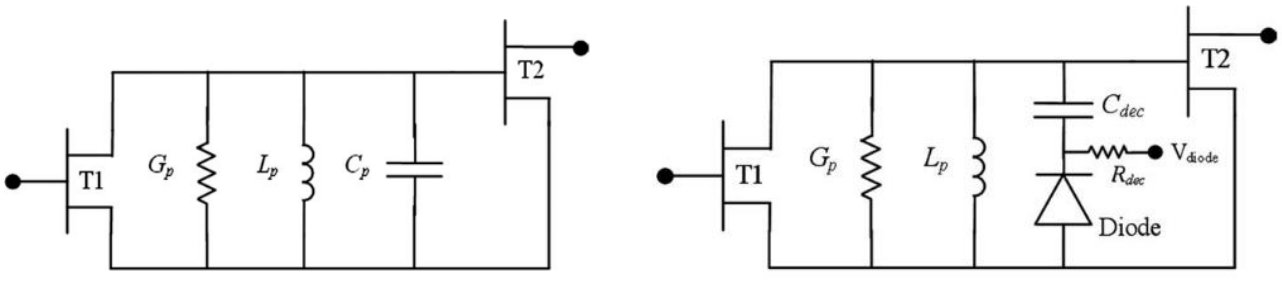

(**a**) (**b**)

Figure 11. The basic cell topology for the fixed-frequency (**a**) and for the tunable (**b**) filter from [5]. Reproduced with permission from [5].

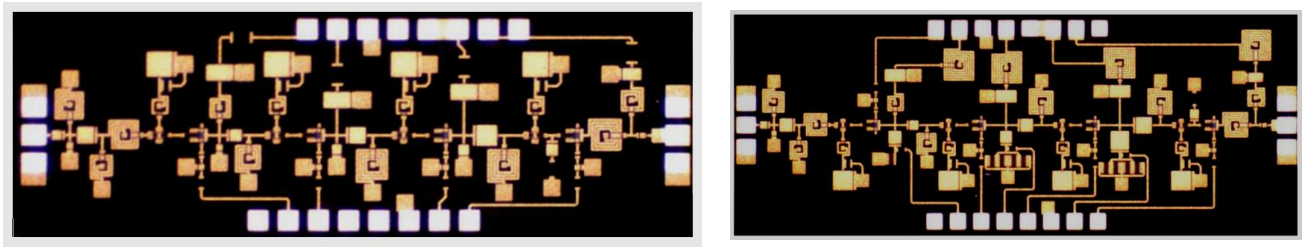

(**a**) (**b**)

Figure 12. The fixed-frequency (**a**) and tunable (**b**) filters from [5]. Reproduced with permission from [5].

The measured S-parameters of the fixed-frequency filter are shown in Figure 13. A 1.7 GHz bandwidth at 11.7 GHz with very good selectivity, a good input match, and a degraded output match, is shown. An 18 dB gain is obtained, with a −14 dBm input-referred compression point. The noise figure is approximately 5 dB. The flat band is obtained by careful optimization of the bias voltages of the transistors of the individual stages that tune the gain of the single blocks.

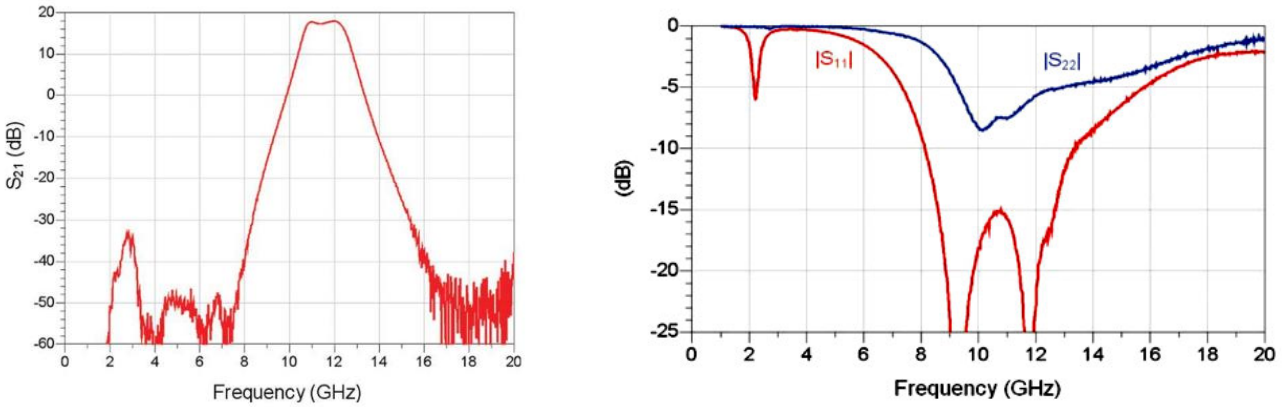

(**a**) (**b**)

Figure 13. The S-parameters of the fixed-frequency filter from [5]: S21 (**a**) and S11 and S22 (**b**). Reproduced with permission from [5].

The measured S-parameters of the tunable filter are shown in Figure 14. The center frequency of the filter can be tuned from 10.6 GHz to 12.8 GHz, with a constant 10 dB gain and a reasonably flat band. The selectivity is again very good, with a slight bandwidth and ripple variation with tuning. The input match is better than 10 dB, while the output match

is badly degraded. The noise figure is again approximately 5 dB, while the input-referred compression point is degraded to −20 dBm due to the presence of the varactors. Again, careful optimization of the bias voltages of the transistors of the individual stages was performed.

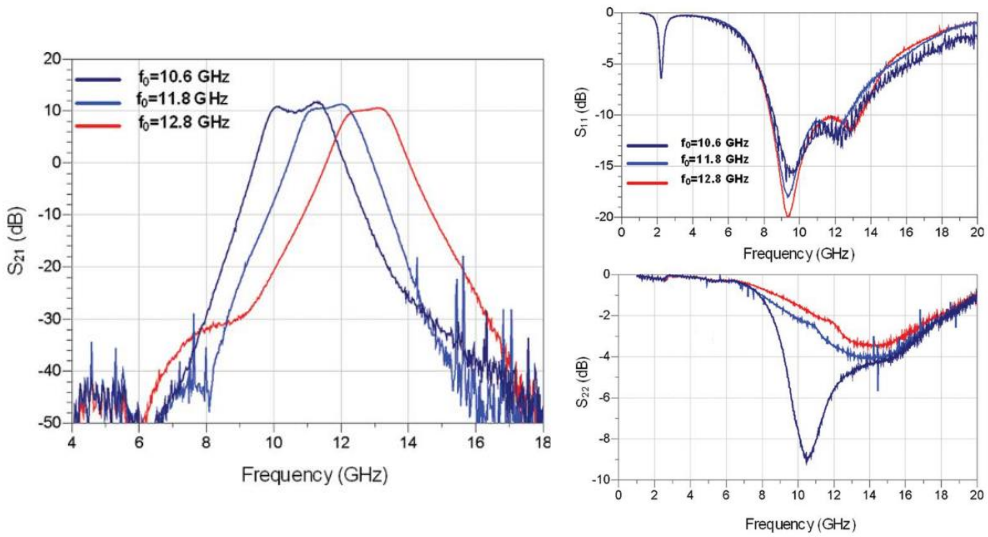

(**a**) (**b**)

Figure 14. The S-parameters of the tunable filter from [5]: (**a**) S21 and (**b**) S11 and S22. Reproduced with permission from [5].

The second example of a tunable cascaded filter is presented in [6] in 2000. The filter is designed at a low frequency (1–1.5 GHz) and in hybrid technology.

The topologies of the passive tunable filtering section and of the active gain block are shown in Figure 15. The complete filter includes two passive sections and a central active gain block. The complete layout and the simulated and measured transfer function of the filter for the two extreme tuning frequencies are shown in Figure 16. The center frequency of the lower tuning frequency is wrongly indicated as 1.602 GHz; it is probably 1.062 GHz. The tuning range is remarkable (515 MHz) with a very constant bandwidth, and good selectivity. The losses vary by approximately 4 dB between the two extremes, but we believe it could be compensated for by a suitable gain slope of the active gain block. Unfortunately, no information is given on the noise and compression performances of the filter, and also (as usual) on the output match.

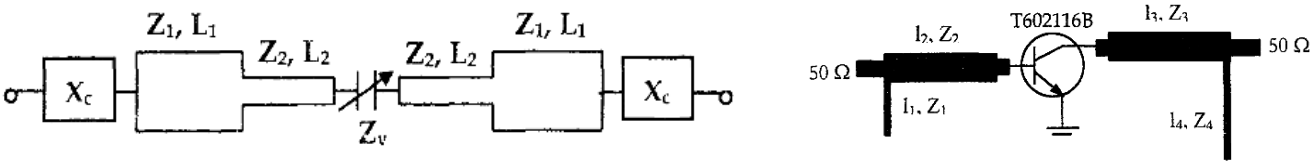

(**a**) (**b**)

Figure 15. The topology of the passive tunable filtering section (**a**) and of the active gain block (**b**) from [6]. Reproduced with permission from [6].

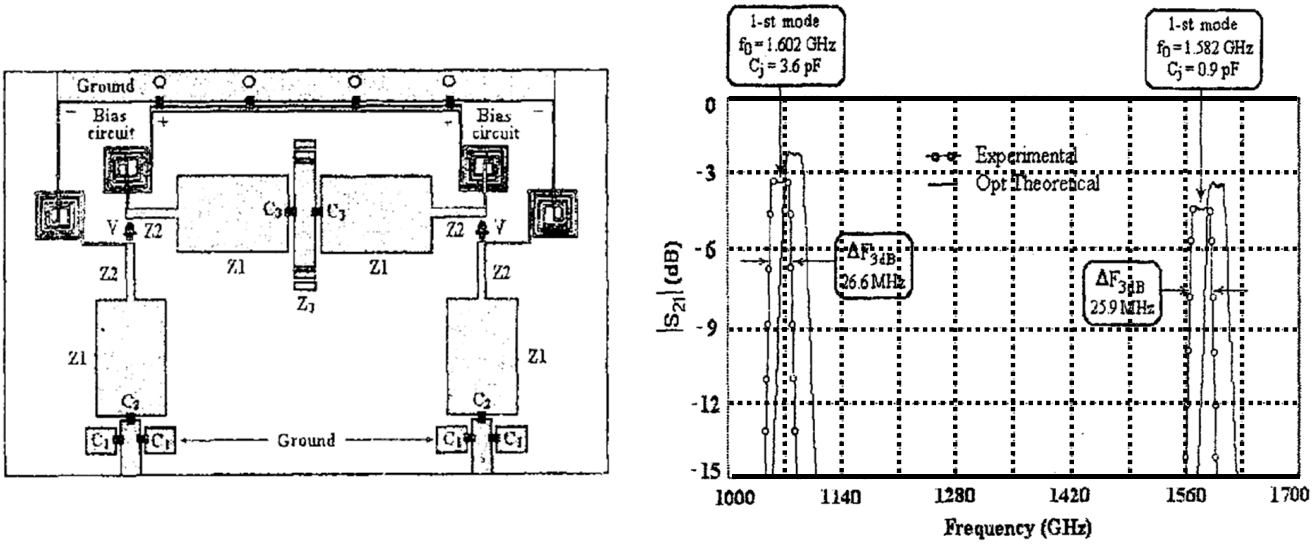

(**a**) (**b**)

Figure 16. The complete layout (**a**) and the simulated and measured transfer function for the two extreme tuning frequencies (**b**) of the filter from [6]. Reproduced with permission from [6].

2.2. Recursive Filters

The basic structure of recursive filters is based on an approach used for digital filters. A general flow chart is shown in Figure 17, where a_n indicates the n-feed-forward branch, b_n indicates the n-feed-back branch, and τ is a delay parameter. Only some of the branches are present in practical microwave implementations. The delay is usually implemented by means of a transmission line and nodes are typically implemented with couplers. In active filters, some elements are active, providing the required loss compensation and selectivity.

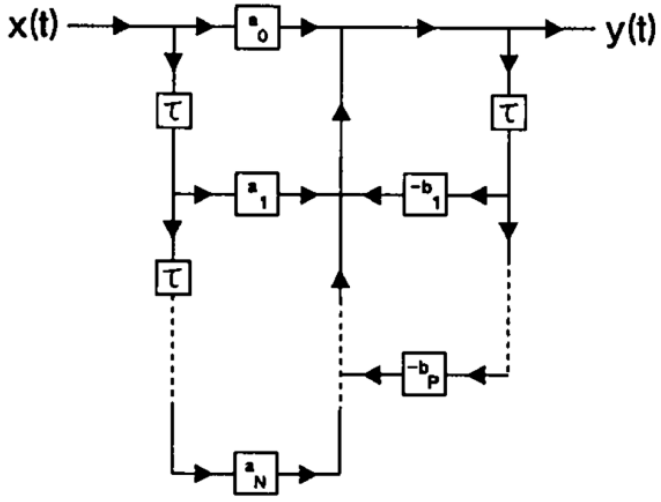

Figure 17. General recursive filter topology [7]. Reproduced with permission from [7].

A fixed-frequency recursive filter has been presented in [8] in 1996. A two-cell topology and a four-cell filter obtained by cascading four single-cell chips are shown in Figure 18. The measured S-parameters are shown in Figure 19, with a 4 dB gain and good input and output match, but poor passband flatness and selectivity. The noise figure is 10 dB and the compression point is 0 dBm.

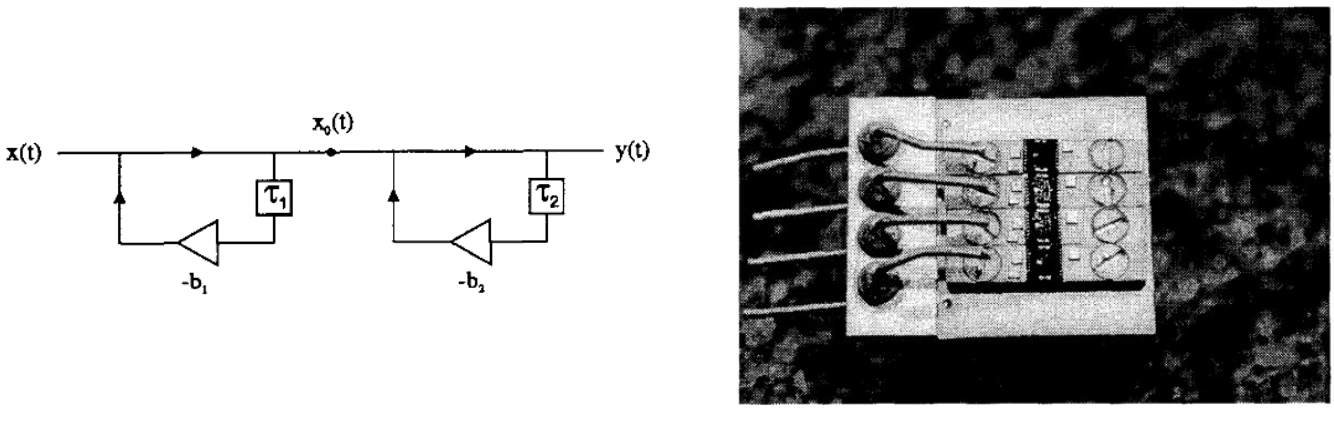

Figure 18. The two-cell topology (**a**) and a four-cell filter obtained by cascading four single-cell chips (**b**) from [8]. Reproduced with permission from [8].

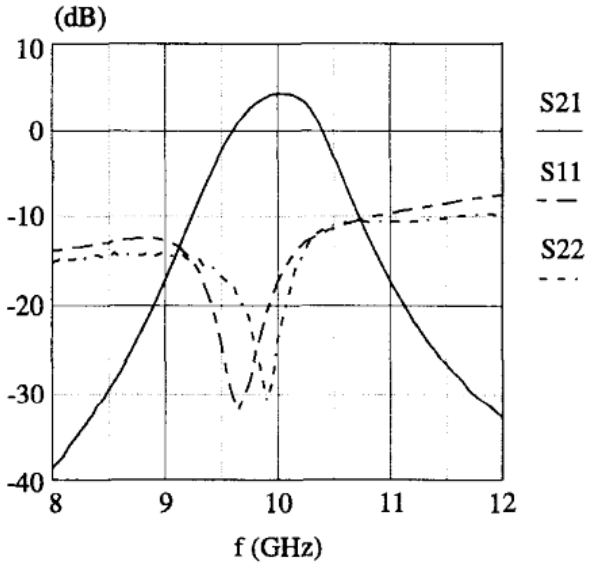

Figure 19. The measured S-parameters of the four-cell filter from [8]. Reproduced with permission from [8].

A sub-class of recursive filters are transversal filters. A general topology is shown in Figure 20. Only fixed-frequency implementations have been published and therefore only one example is presented here [9] from 1989, with an implementation in GaAs MMIC technology. The structure of the filter is also shown in Figure 20, together with its schematic. A picture of the fabricated chip is shown in Figure 21, together with its measured S-parameters. The filter has a 2 dB loss at 10.5 GHz with 1 dB ripple, good selectivity, and a reasonably good match. No information is given on the noise figure and compression. No hint is given on potential tunability either.

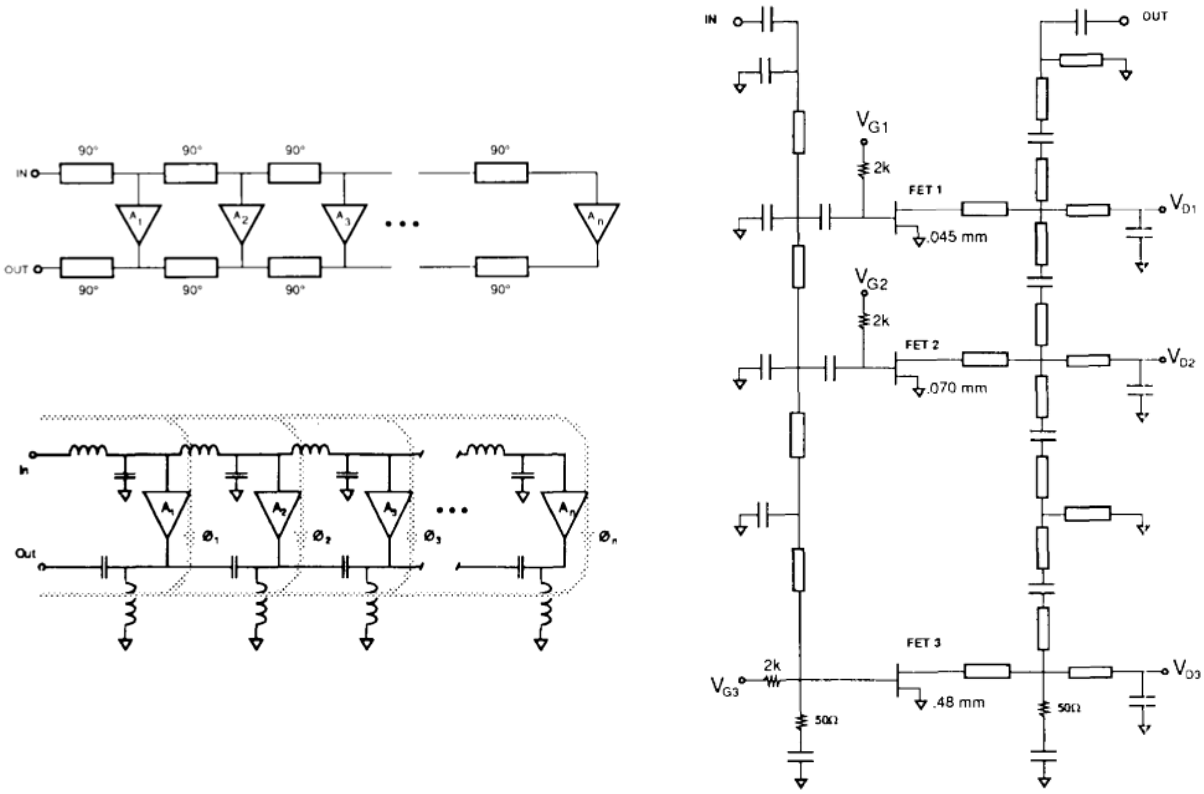

(**a**) (**b**)

Figure 20. The general topology ((**a**)-upper), the structure ((**a**)-lower), and the schematic (**b**) of the transversal filter from [9]. Reproduced with permission from [9].

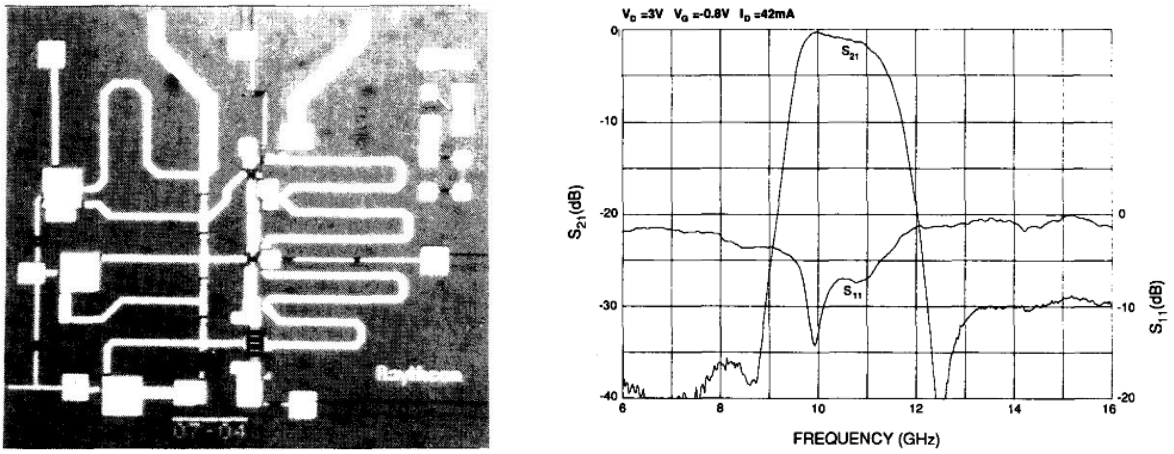

(**a**) (**b**)

Figure 21. The chip photograph (**a**) and the measured S-parameters (**b**) of the transversal filter from [9]. Reproduced with permission from [9].

An example of a tunable GaAs MMIC recursive filter is presented in [10], in 1990. The flow chart is shown in Figure 22a, and the principle of operations is shown in Figure 22b. $T_1(S)$ and $T_2(s)$ are the total transfer functions of *LPF1* and *LPF2*, respectively, while a_1, a_2, b_1, and b_2 are their coefficients, as obtained in [10]. The schematic of the designed chip is shown in Figure 23a, and the photograph of the chip is shown in Figure 23b. The complete filter is composed of two identical cascaded chips.

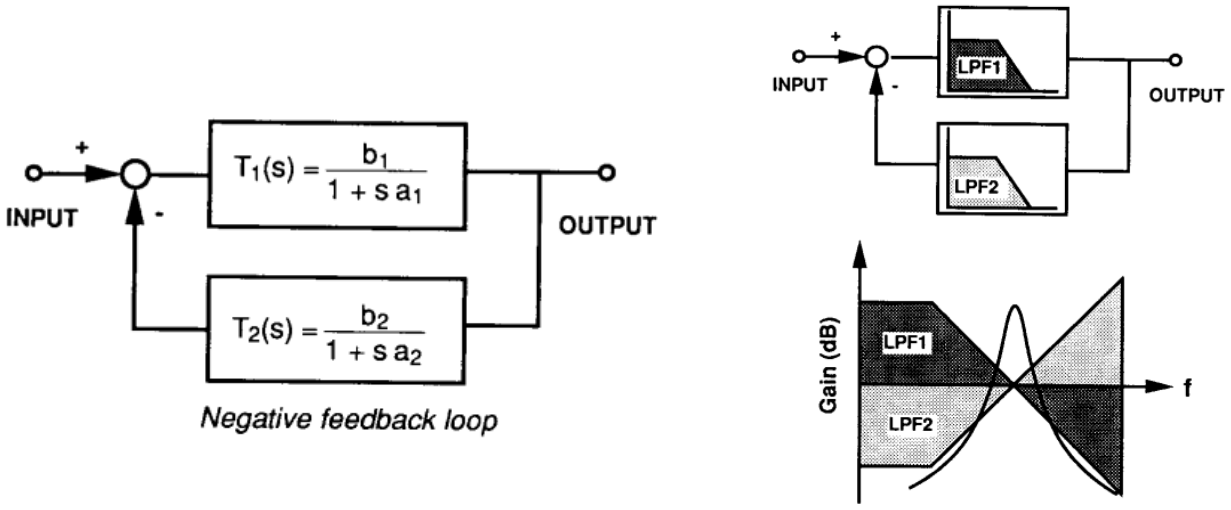

(**a**) (**b**)

Figure 22. The flow chart (**a**) and the principle of operations (**b**) of the filter from [10]. Reproduced with permission from [10].

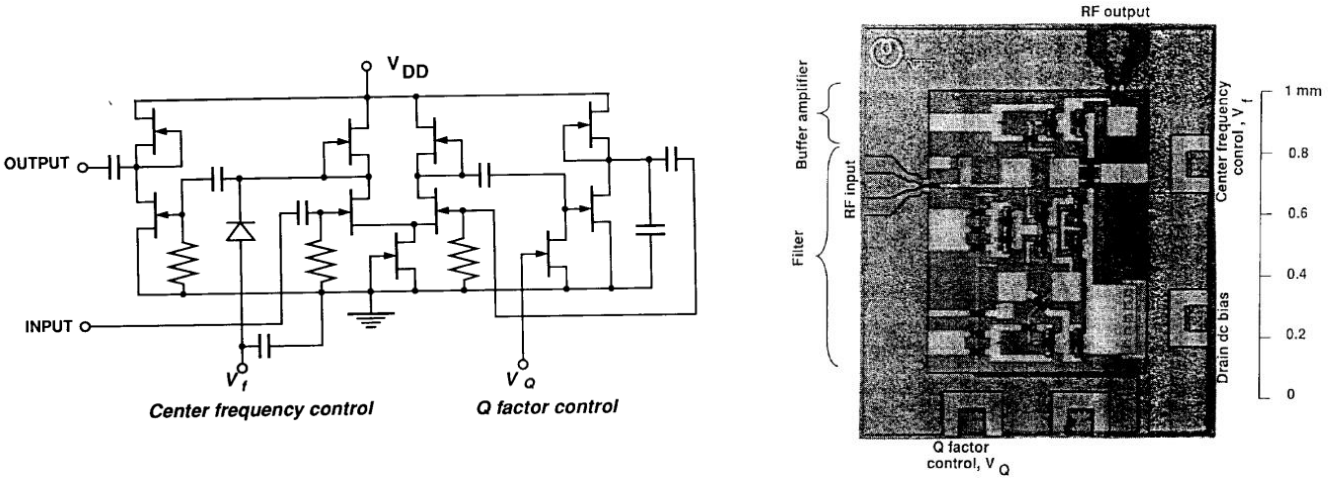

(**a**) (**b**)

Figure 23. The schematic (**a**) and the photograph (**b**) of the filter from [10]. Reproduced with permission from [10].

The center frequency and the Q-factor of the filter can be independently controlled, as can be seen in Figure 24, by means of a varactor and a varistor, respectively. The transfer function of the complete filter for three different tuning states (*a*,*b*,*c*) is shown in Figure 25: the filter has good tunability (more than 100 MHz), it shows good selectivity (a quality factor between 20 and 200) and in-band flatness (flatness within 0.7 dB), it has a high gain, and also a high gain variation with the tuning. Nothing is said about matching, noise, or compression.

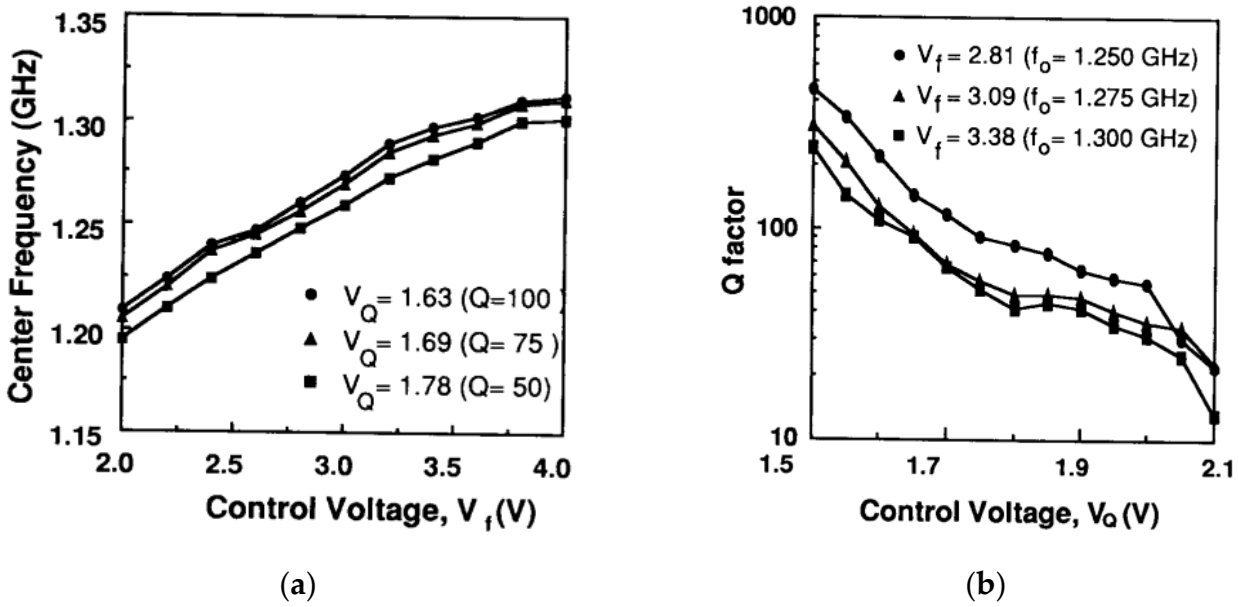

Figure 24. The center frequency (**a**) and Q-factor (**b**) control laws of the filter from [10]. Reproduced with permission from [10].

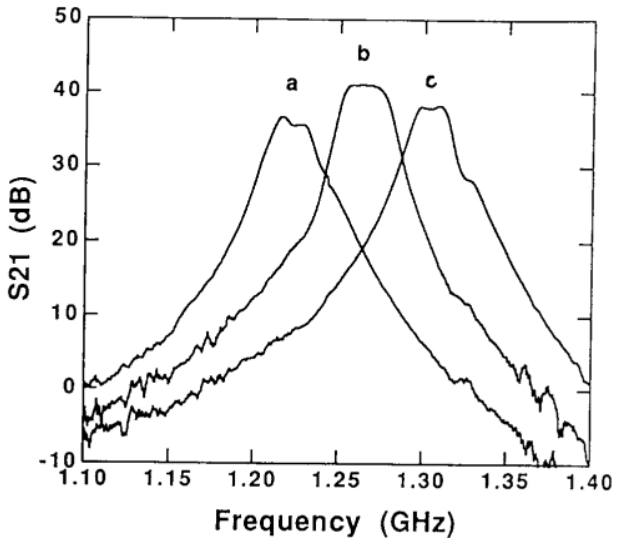

Figure 25. The transfer function of the filter for three different tuning states (*a*,*b*,*c*), from [10]. Reproduced with permission from [10].

An example of implementation as GaAs MMIC from 2002 is presented in [11]. The general structure is shown in Figure 26a, where the four filters are internally recursive, and the chip photograph is shown in Figure 26b. The measured transfer function of the filter for eight tuning states is shown in Figure 27. Tuning in the 7.9–9.7 GHz is obtained, with a high gain ($\geq$10 dB) but large gain variation (approximately 5 dB), poor selectivity, and an input and output match better than 10 dB. The measured noise is 6 dB, with an IIP3 of 0 dBm for all tuning states. As can be seen, results are not very encouraging in term of the insertion loss variation and shape factor.

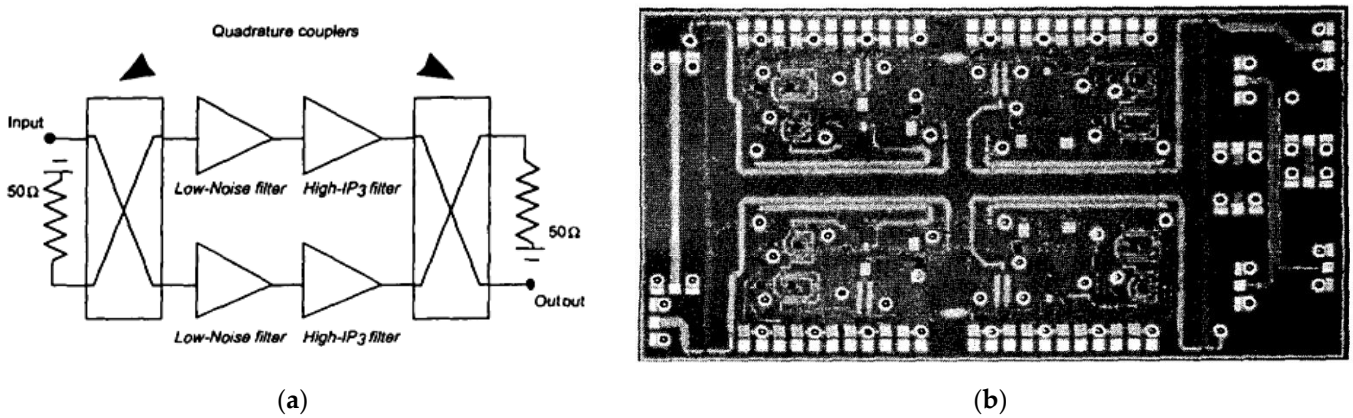

(**a**) (**b**)

Figure 26. The general structure (**a**) and chip photograph (**b**) of the filter from [11]. Reproduced with permission from [11].

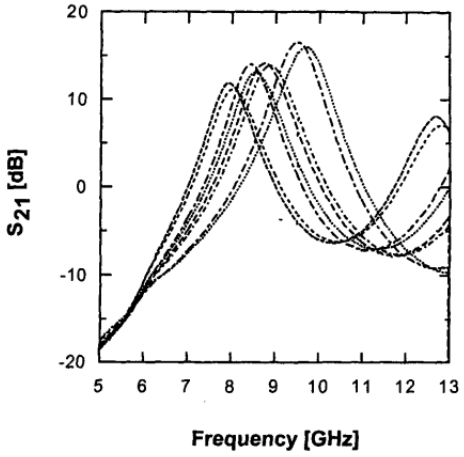

Figure 27. The measured transfer function of the filter from [11] for several tuning states. Reproduced with permission from [11].

Another example of a tunable recursive filter is presented in [12] in 1992, but in a hybrid implementation. The structure of the single section and a picture of the three-section complete filter are shown in Figure 28. The resonant frequency of the half-wavelength resonator is tuned by the varactor, while the active loop, coupled through two quarter-wavelength couplers and including an amplifier, an attenuator, and a phase shifter, increases the Q-factor of the resonator.

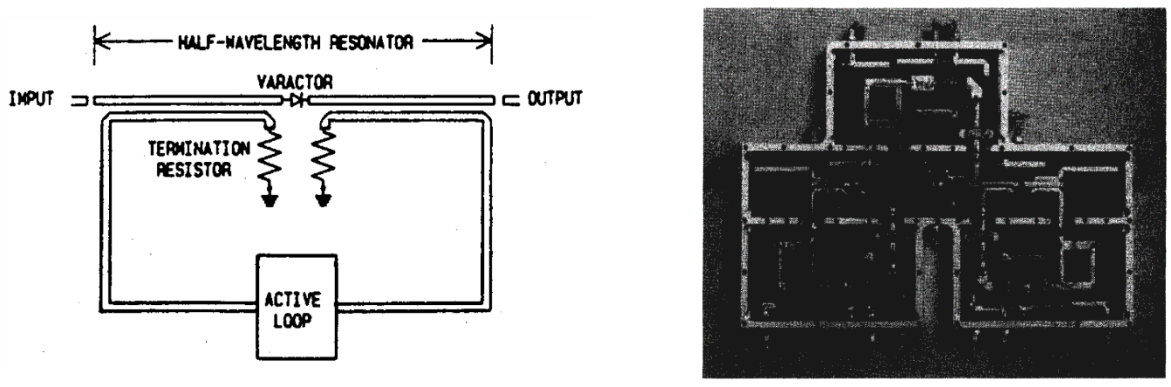

(**a**) (**b**)

Figure 28. The structure of the single section (**a**) and the complete filter (**b**) from [12]. Reproduced with permission from [12].

The measured transfer function and noise figure are shown in Figure 29. The filter has zero attenuation, very good selectivity (approximately 20 dB at 50 MHz from the central frequency), a better than 20 dB input and output match, and is tunable in the range 3.6–3.8 GHz. The noise figure shown in Figure 29 refers to the filter tuned at 3.69 GHz center frequency and is approximately 15 dB within the passband. The compression point is −4 dBm (Figure 30a). The temperature dependence (Figure 30b) indicates that an external variable element is required for practical applications.

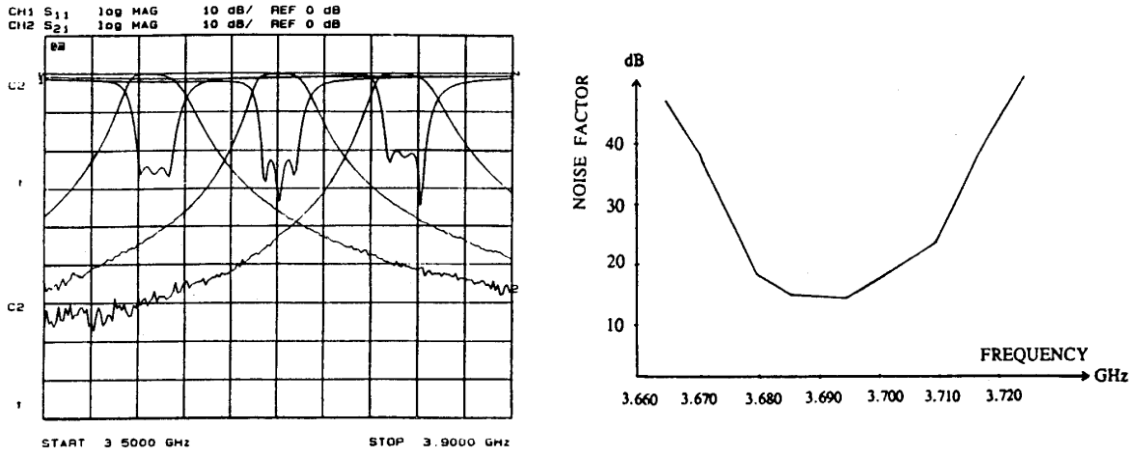

(**a**) (**b**)

Figure 29. The measured transfer function (**a**) and noise figure (**b**) of the filter from [12]. Reproduced with permission from [12].

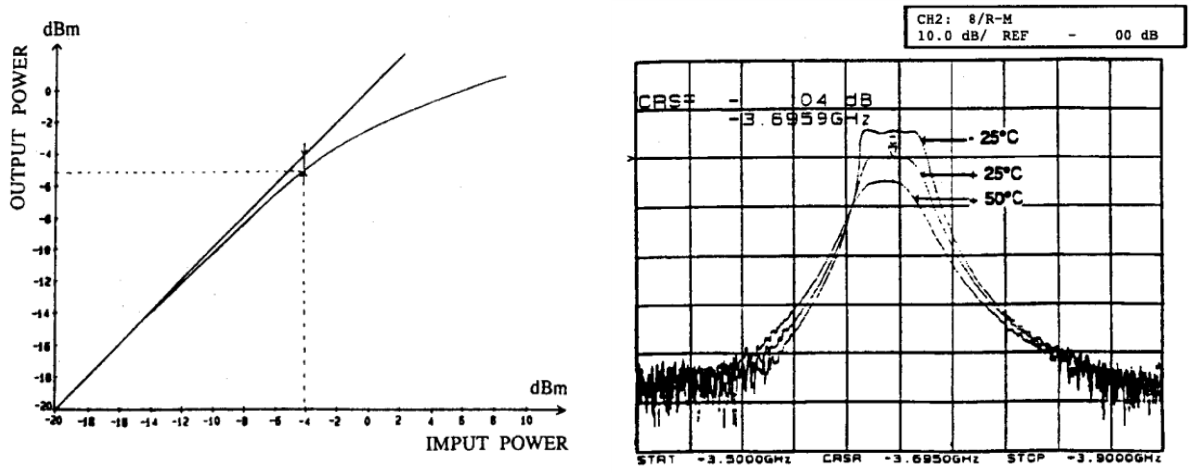

(**a**) (**b**)

Figure 30. The measured compression curve (**a**) and temperature dependence (**b**) of the filter from [12]. Reproduced with permission from [12].

However, it must be remarked that it is difficult to make an MMIC implementation of this filter because of the large dimensions (Figure 28a) and high losses of the lines on a chip.

A final example of a tunable recursive single-cell filter in GaAs MMIC technology is presented in [13] in 1995. The topology of the cell is shown in Figure 31, together with its electrical schematic. The chip layout is shown in Figure 32, together with the measured transfer function. The tunability is limited and the gain variation is large. The results are not very promising considering the results shown in Figure 32b.

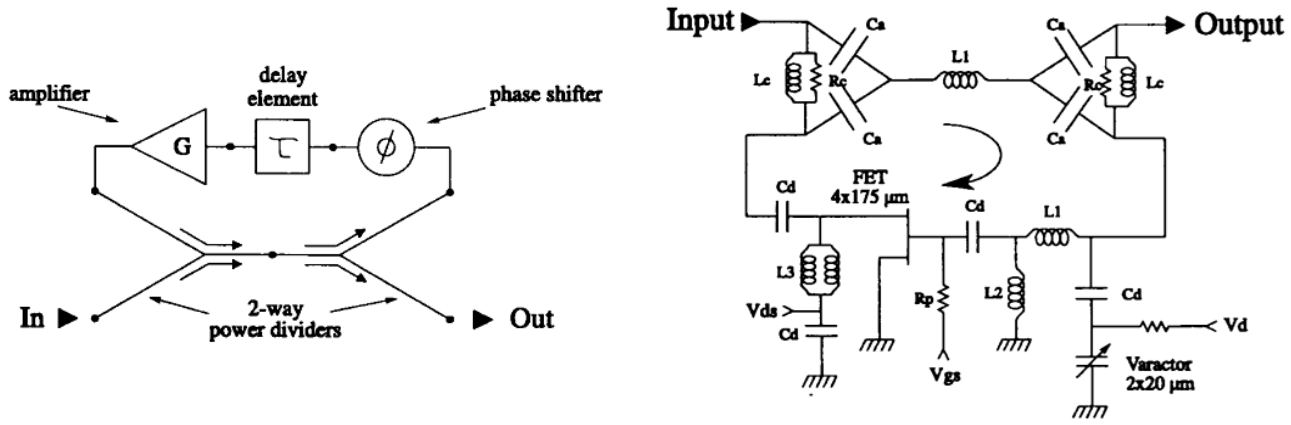

(**a**) (**b**)

Figure 31. The topology (**a**) and the electrical schematic (**b**) of the single-cell filter from [13]. Reproduced with permission from [13].

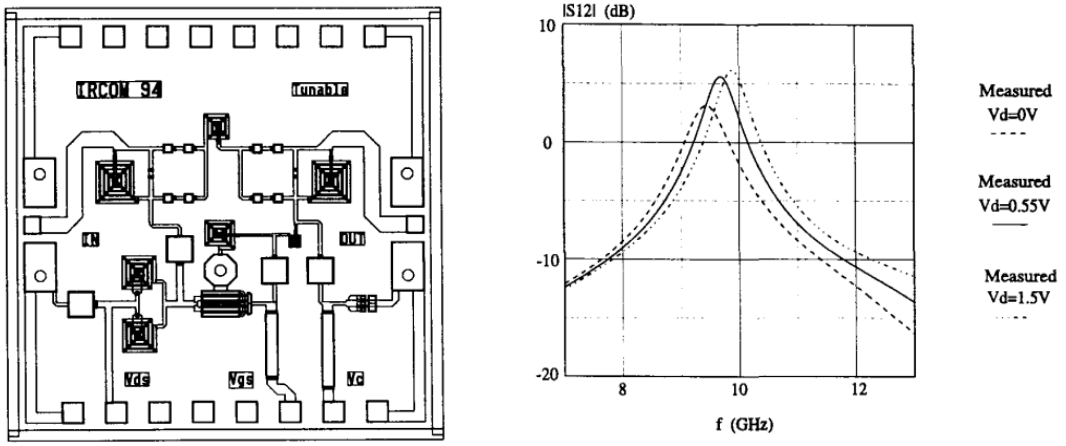

(**a**) (**b**)

Figure 32. The layout (**a**) and the measured transfer function (**b**) of the single-cell chip from [13]. Reproduced with permission from [13].

Overall, the performances of the published recursive filters are not very encouraging. A limited tunability, excessive gain variations, or limited selectivity are present in all of the published implementations, dating back to more than 20 years ago. No successful recent work has been done with this approach, and no work at high frequencies.

3. Filters Based on the Use of Components with Negative Resistive Part

3.1. Cascaded Filters

The basic structure of a negative-resistance filter consists of passive filters, fixed-frequency or tunable, distributed or lumped, with an added negative-resistance component for loss compensation. The value of the negative resistance can be fixed or tunable, for Q-factor adjustment or tuning. The imaginary part of the negative-resistance component, if present, is included in the passive filter as a parasitic reactance. The negative-resistance component is a transistor, FET or BJT, which is potentially unstable in the band of interest (and only there), with two terminals loaded in such a way as to make it unstable (if not already so), and the third one is used as the access port with negative resistance.

Implementations have been presented both in hybrid and in monolithic form, both fixed-frequency and tunable. Typical solutions are presented for all available approaches.

Results based only on simulations are not included, given the critical role of fabrication and stability issues. Most examples are more than 20 years old, with only the BiCMOS and CMOS implementations being more recent. For older implementations, little information is available, and, in particular, noise and power handling are usually not reported.

The first example, from 1993, demonstrates a hybrid filter approach with distributed passive filtering structures and a negative resistance [14]. The negative-resistance component is implemented as an MMIC, to be inserted in the hybrid layout. Its schematic is shown in Figure 33, together with the chip photograph and measured resistance. The same architecture has then also been reproposed in [15].

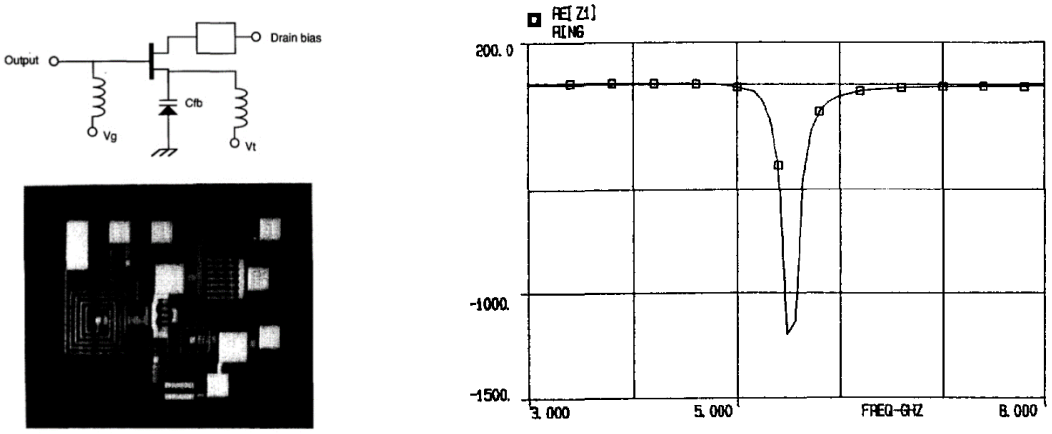

(**a**) (**b**)

Figure 33. Schematic (upper **a**), chip picture (lower **a**) and measured resistance (**b**) of the negative-resistance component from [14]. Reproduced with permission from [14].

Two filters are realized with this technique. The first one is an end-coupled resonator filter, with added negative resistances for the compensation of the resonator losses. The layout is shown in Figure 34 together with its transmission response. The filter has a 2 dB insertion loss, with a ± 0.6 dB ripple and excellent selectivity (approximately 13 dB at 10 MHz from the central frequency).

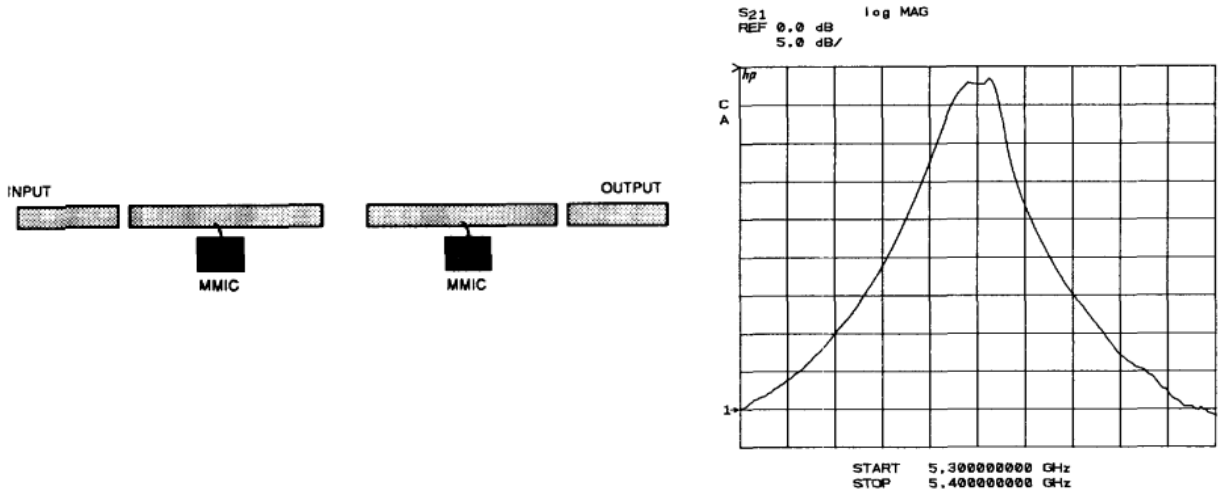

(**a**) (**b**)

Figure 34. Layout (**a**) and measured transfer function (**b**) of the end-coupled resonator filter from [14]. Reproduced with permission from [14].

The second filter is a dual-mode ring resonator filter. The layout is shown in Figure 35 together with the measured S-parameters. The filter has a 1 dB gain with a good match (10 dB) and selectivity (approximately 11 dB at 10 MHz from the central frequency). The two-tone response is shown in Figure 36, indicating a two-tone compression point of −8 dBm.

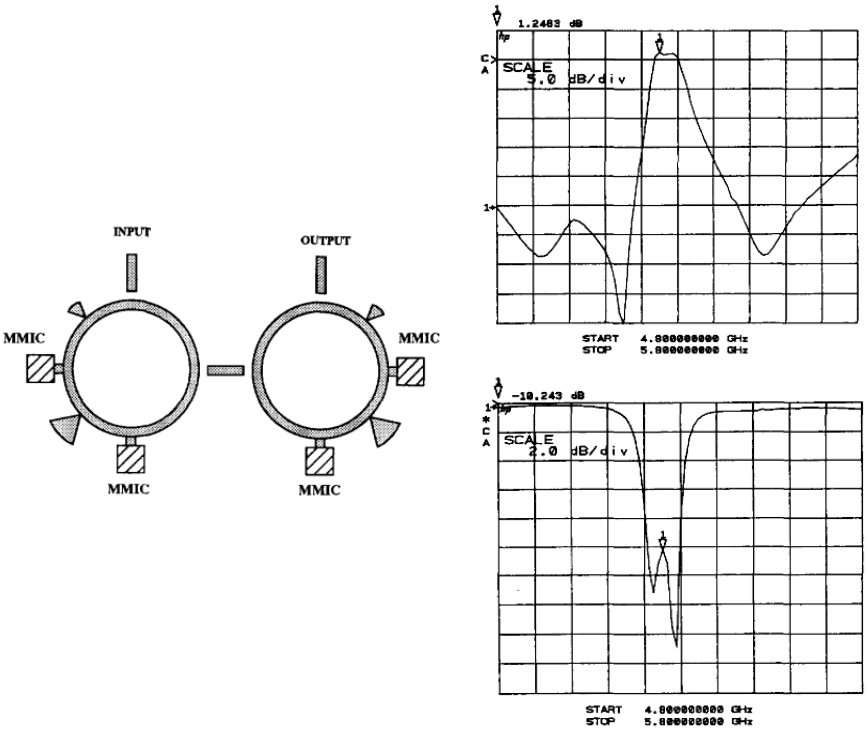

(**a**) (**b**)

Figure 35. Layout (**a**) and measured S-parameters (**b**) of the dual-mode ring resonator filter from [14]. Reproduced with permission from [14].

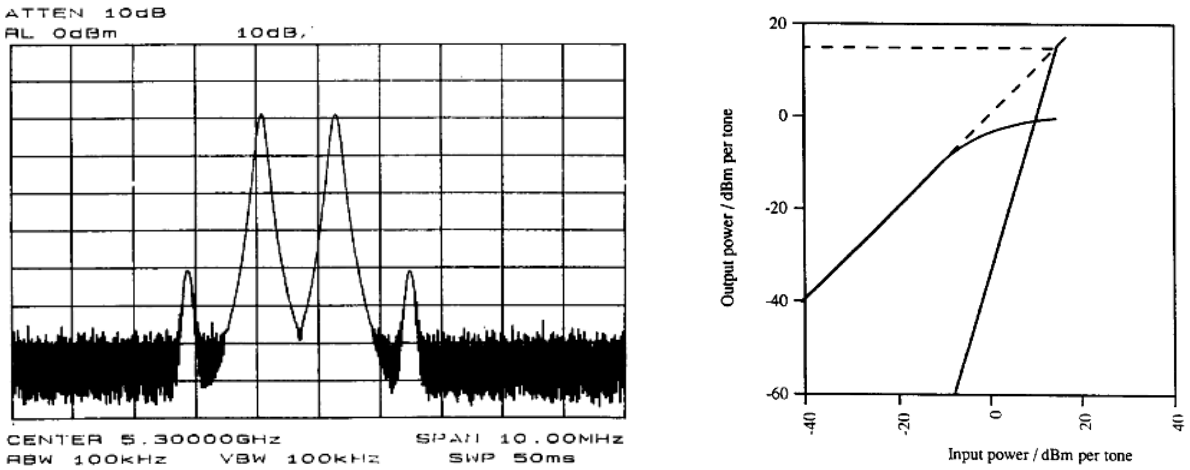

(**a**) (**b**)

Figure 36. Output spectrum for a −20 dBm two-tone input (**a**) and compression curve (**b**) of the dual-mode ring resonator filter from [14]. Reproduced with permission from [14].

A second example, from 1997, is a hybrid distributed filter at 3.9 GHz with discrete transistors acting as negative-resistance elements [16]. The simplified schematic is shown in Figure 37 together with the layout. In Figure 38, the measured and simulated S-parameters are presented. The filter has zero losses, a good match (−15 dB at the input and −10 dB at the output), and excellent selectivity (35 dB isolation at 140 MHz offsets) and passband flatness (<0.2 dB). No information on the noise figure or gain compression is available.

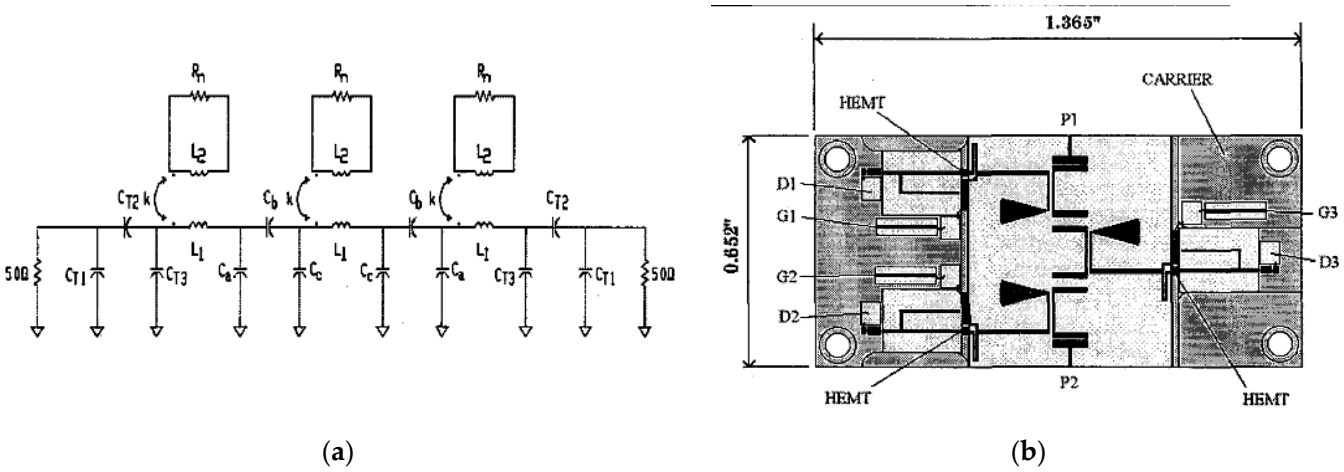

(**a**) (**b**)

Figure 37. Simplified schematic (**a**) and layout (**b**) of the hybrid filter from [16]. Reproduced with permission from [16].

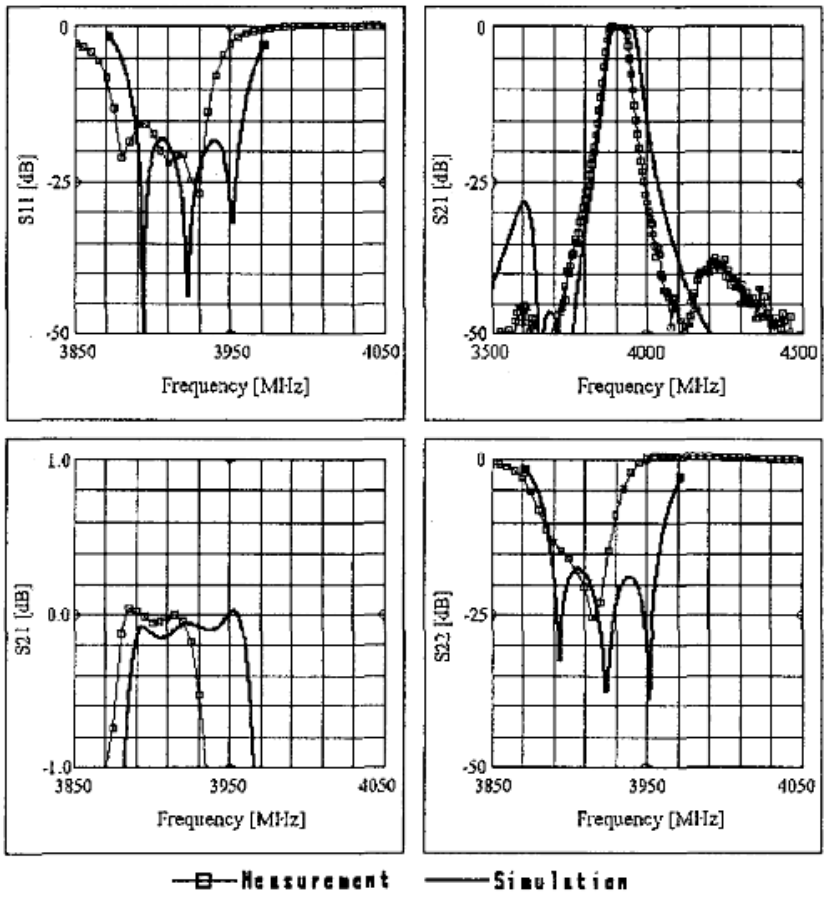

Figure 38. S-parameters of the hybrid filter from [16]. Reproduced with permission from [16].

A fixed-frequency example from 1995 in MMIC technology has been published in [17]. The negative-resistance component is a FET with a capacitive series feedback, shown in Figure 39, compensating for the losses of a tunable LC shunt resonator. A separate chip with the resonator has been fabricated and measured, and is also shown in Figure 39.

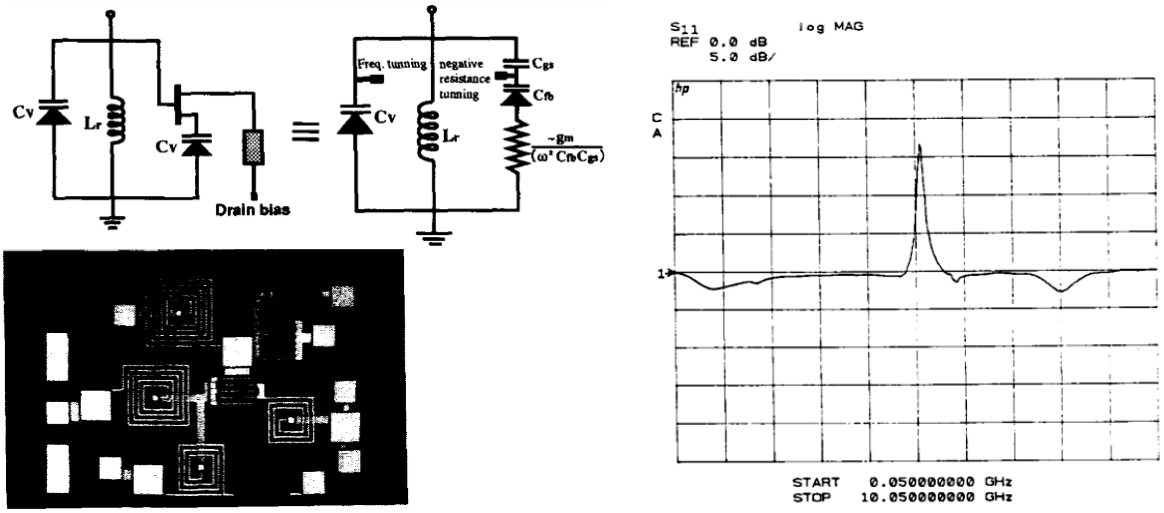

Figure 39. Simplified schematic (**upper left**), chip photograph (**lower left**), and reflection coefficient (**right**) of the negative-resistance resonator from [17]. Reproduced with permission from [17].

A two-resonator filter has been designed at 4.7 GHz. The layout is shown in Figure 40 together with the chip photograph. The measured S-parameters are shown in Figure 41. The filter has zero losses and excellent passband flatness. The tuning capabilities of the resonator have been used to compensate for the fabrication tolerances and to optimize the fixed-frequency performances. No information on the noise figure or compression point is available.

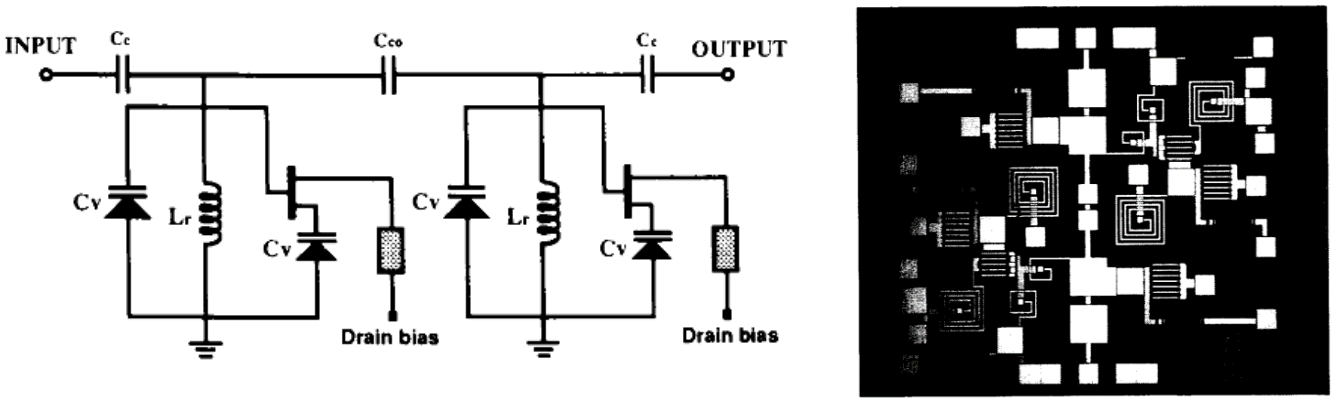

(**a**) (**b**)

Figure 40. Simplified schematic (**a**) and chip photograph (**b**) of the bandpass filter from [17]. Reproduced with permission from [17].

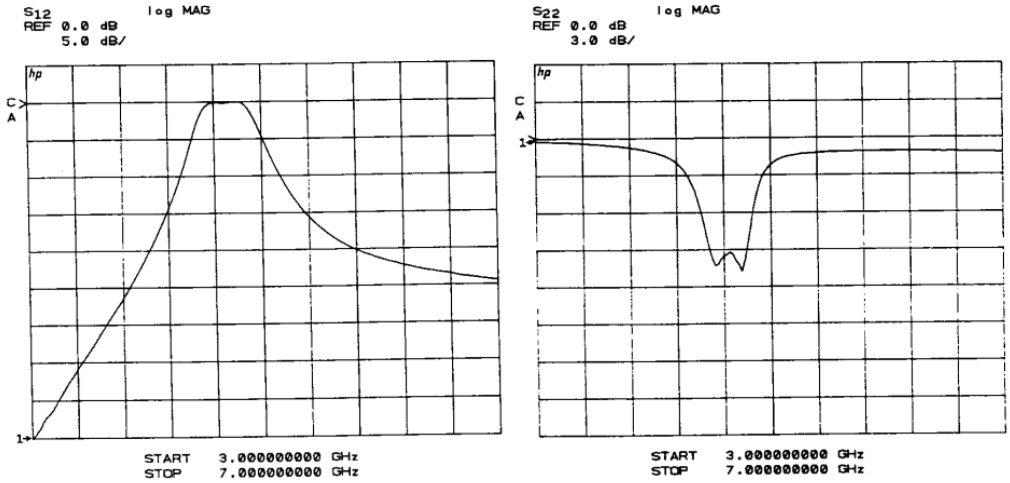

(**a**) (**b**)

Figure 41. S-parameters of the bandpass filter from [17]: (**a**) S12, (**b**) S22. Reproduced with permission from [17].

A more recent fixed-frequency filter from 2008, in 0.18 µm CMOS technology, has been presented in [18]. A Q-enhanced half-wavelength resonator includes a complementary cross-coupled transistor pair in a positive feedback configuration, generating a negative resistance. The simplified schematic with its equivalent circuit and the enhanced Q-factor are shown in Figure 42.

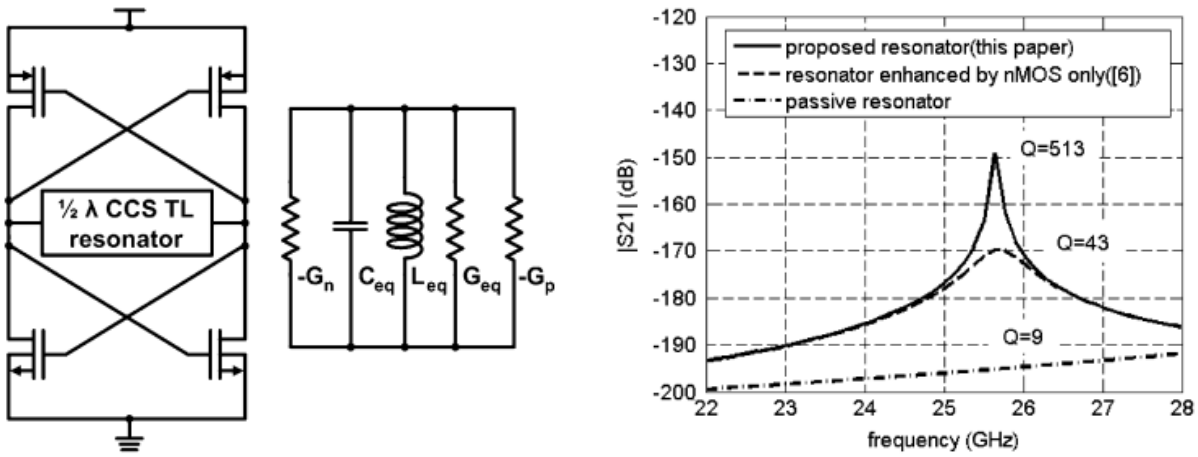

(**a**) (**b**)

Figure 42. Simplified schematic (**a**) and enhanced Q-factor (**b**) of the active resonator from [18]. Reproduced with permission from [18].

A two-resonator filter centered at 22.6 GHz is shown in Figure 43. The simulated and measured S-parameters, the compression point, and the noise figure are shown in Figure 44. The filter has a flat passband with zero losses, and a good selectivity (−10 dB at 1.5 GHz of frequency offset) and match (<10 dB). The compression point is −8 dBm and the noise figure is approximately 14 dB.

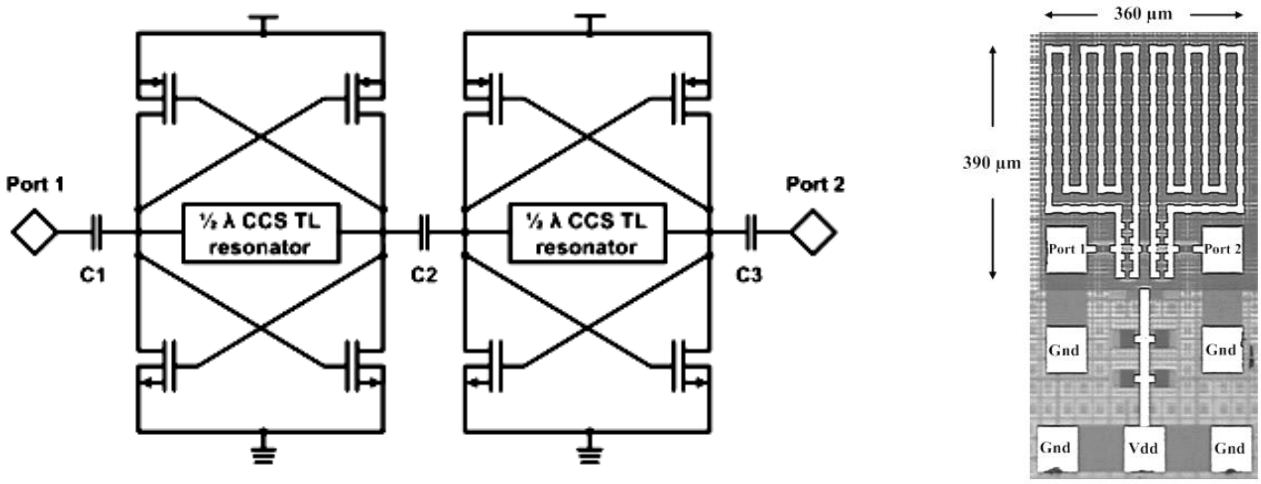

Figure 43. Simplified schematic (**a**) and chip photograph (**b**) of the filter from [18]. Reproduced with permission from [18].

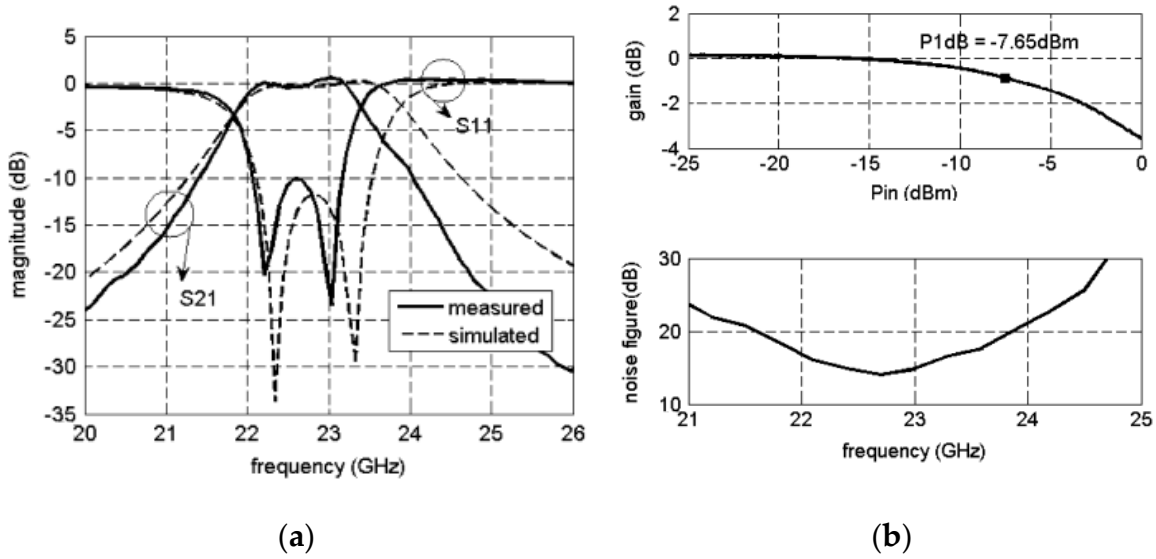

Figure 44. Simulated and measured S-parameters (**a**), compression point and noise figure (**b**) of the filter from [18]. Reproduced with permission from [18].

Another relatively recent fixed-frequency filter at 65 GHz in MMIC technology has been presented in [19] in 2004. The filter is based on a half-wavelength resonator coupled to a negative-resistance component, for loss compensation. The structure of the resonator and the schematic of the negative-resistance component, based on a GaAs HEMT, are shown in Figure 45. The negative resistance and the reactance of the negative-resistance component are shown in Figure 46a for different gate voltages of the HEMT. It is apparent that the negative resistance can be tuned by the gate bias voltage, and so the Q-factor of the resonator, while the reactance stays constant, does not affect the resonant frequency.

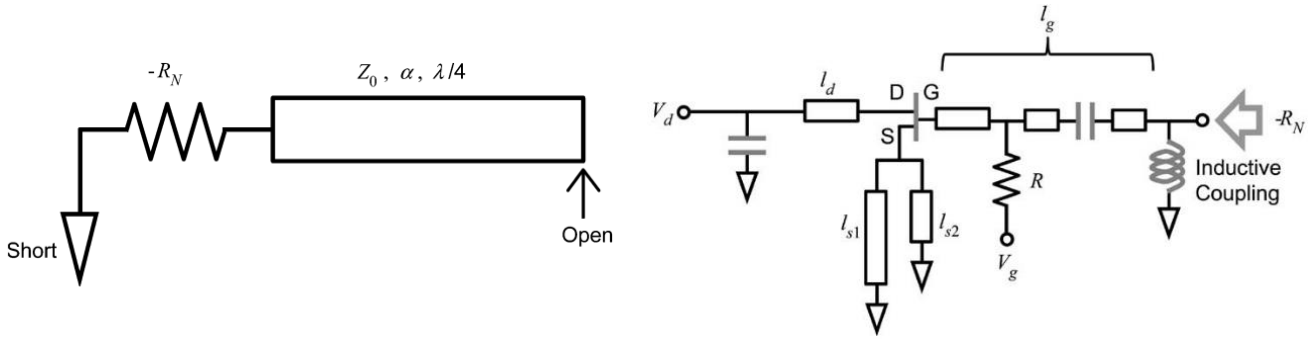

(**a**) (**b**)

Figure 45. The structure of the half-wavelength resonator (**a**) and the schematic of the negative-resistance component (**b**) from [19]. Reproduced with permission from [19].

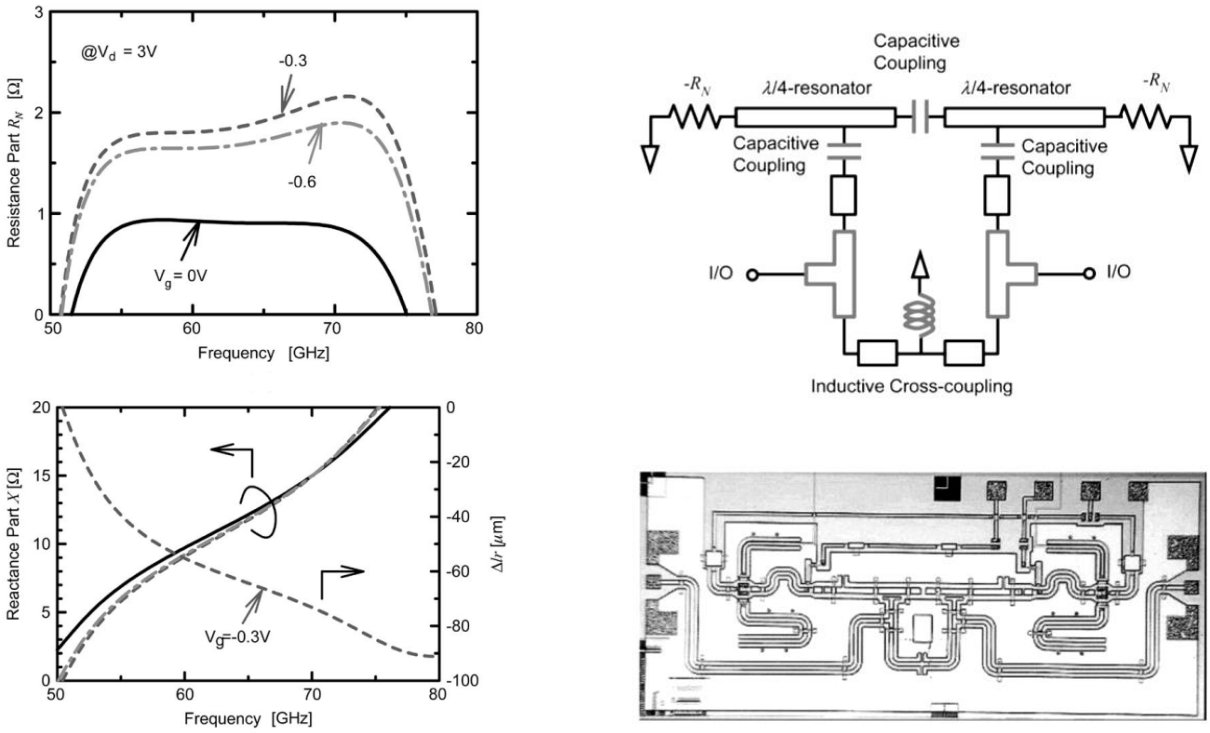

(**a**) (**b**)

Figure 46. The resistive and reactive part of the negative-resistance component (**a**), the structure of the filter ((**b**)—upper), and a chip photograph ((**b**)—lower) from [19]. Reproduced with permission from [19].

The structure of the complete filter together with a photograph of one of the chips are shown in Figure 47b. Two filters have been designed, with different bandwidths: 2% for the transmitter module, and 4% for the receiver module. The measured S-parameters for the two versions are shown in Figure 47.

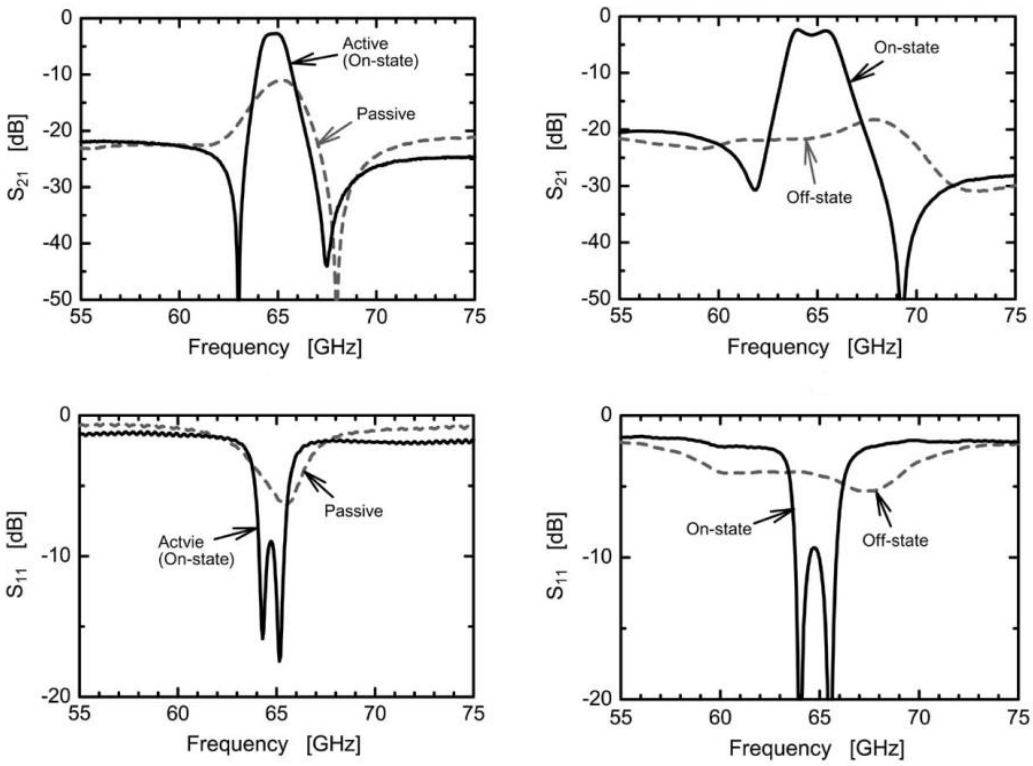

(**a**) (**b**)

Figure 47. The S-parameters of the narrowband (**a**) and of the wideband (**b**) filters with the transistors in the off-state and in the on-state, from [19]. Reproduced with permission from [19].

The compression curve of the narrowband filter for the transmitter module is shown in Figure 48a, showing a 5 dBm compression point. The noise figure for the wideband filter for the receiver module is also shown in Figure 48b: a value above 11 dB was obtained. The effect of the temperature was also measured before and after compensation, my means of automatic gate bias voltage adjustment (Figure 49).

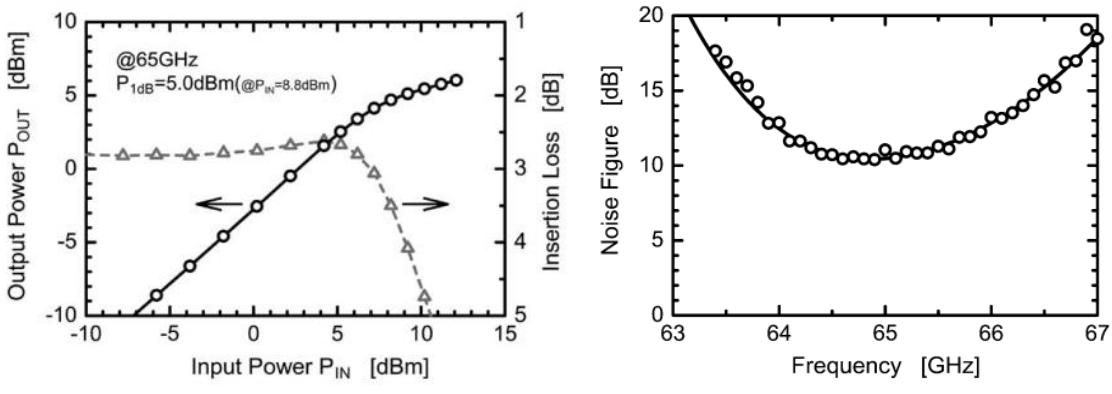

(**a**) (**b**)

Figure 48. The compression curve of the narrowband filter (**a**) and the noise figure of the wideband filter (**b**) from [19]. Reproduced with permission from [19].

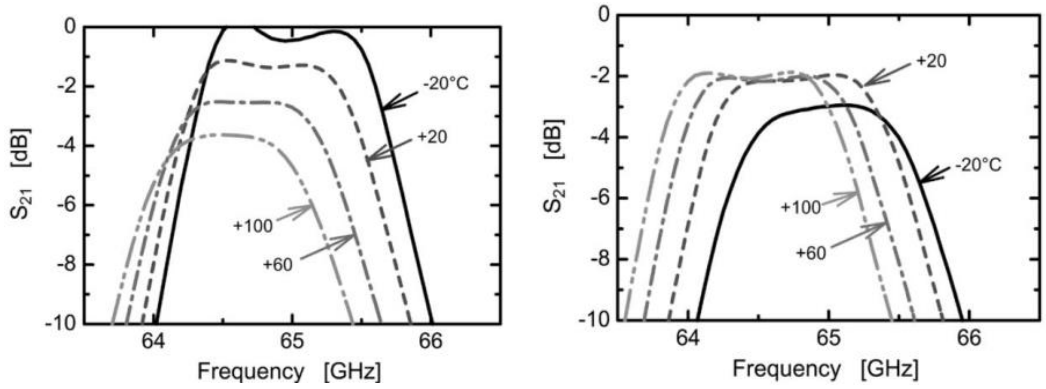

Figure 49. The transfer function of the wideband filter with the temperature as a parameter without (**a**) and with compensation (**b**), from [19]. Reproduced with permission from [19].

Thus far for fixed-frequency implementations, similar conclusions to the cascaded filters can be drawn. Selectivity is the main asset of this type of filter, with potentially good power handling and a manageable noise figure if preceded by a low-noise amplifier.

There are only a few examples of tunable negative-resistance filters in the literature: we will review them all.

The first one is a hybrid filter dating back to 1990 [20], and is based on a varactor-tuned active tank circuit at 10 GHz (Figure 50a). A complete filter includes more than one resonating tank (Figure 50b). The negative resistance is implemented via a potentially unstable transistor; its resistive and reactive parts are shown in Figure 51a. The reactive part is almost zero at the center frequency of the filter (10 GHz). The S-parameters of the filter are shown in Figure 51b. The filter has good tunability (430 MHz) and selectivity, and a reasonably good match (<−5 dB) and passband flatness (<1 dB). However, the return loss is negative near the edges of the passband, thus creating potential instability. This is a common feature of many active filters and is usually removed by careful design. The compression point is approximately −15 dBm. No information is given on the noise figure.

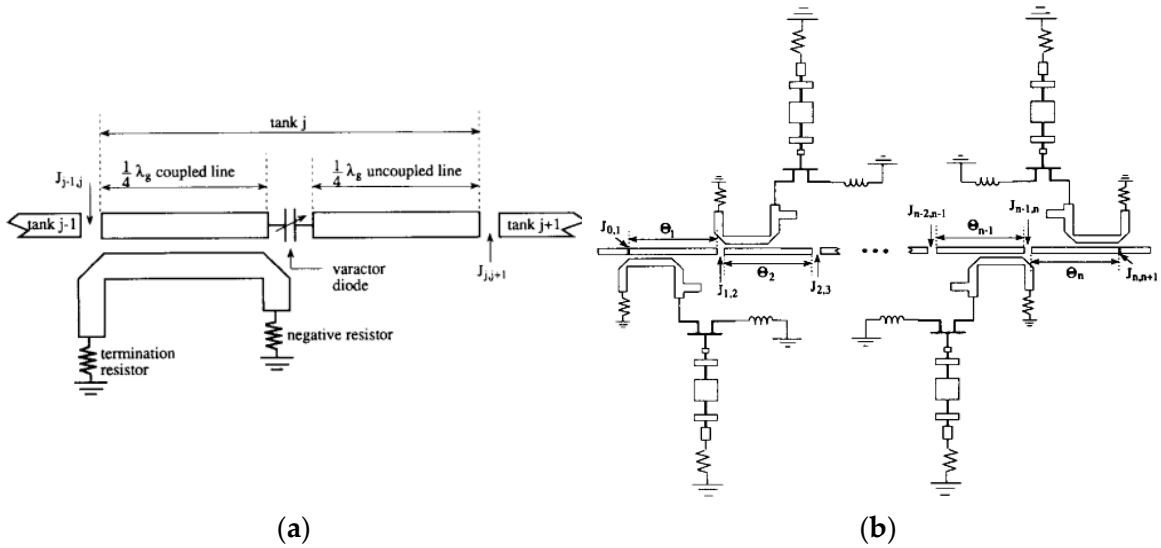

Figure 50. The varactor-tuned active tank circuit (**a**) and the complete filter (**b**), from [20]. Reproduced with permission from [20].

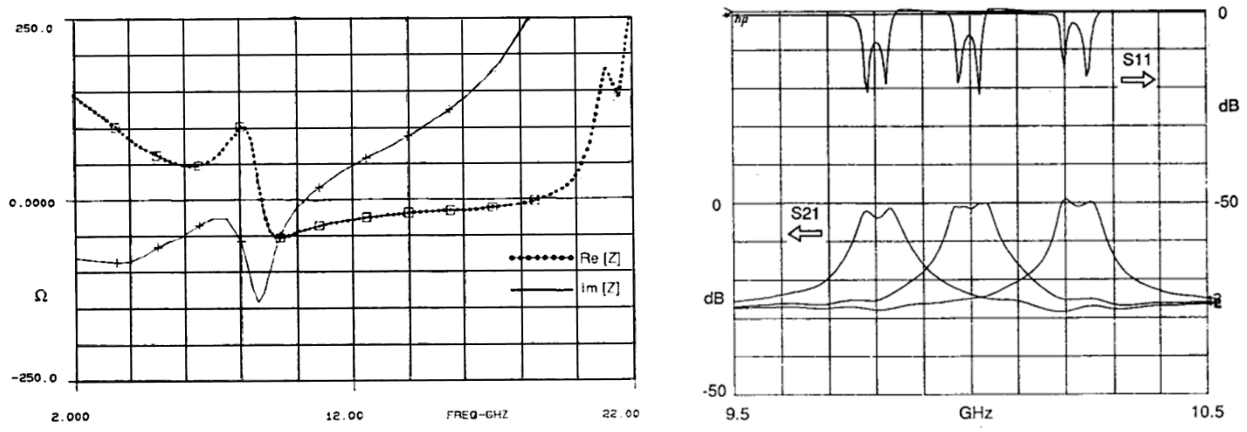

(**a**) (**b**)

Figure 51. The calculated real and imaginary parts of the negative-resistance component (**a**) and the measured S-parameters of the complete filter (**b**), from [20]. Reproduced with permission from [20].

The second example is again a hybrid filter at 1.8 GHz based on a varactor-tuned combline network [21]. The layout and the measured S-parameters of the filter are shown in Figure 52. The negative resistance is provided by a common-collector transistor with a base network resonating at the center frequency of the filter, thus providing instability only in the tuning band of the filter. The filter has very good tunability (1.4–2.2 GHz), a flat passband, and a good match (<−15 dB) and selectivity, but both the bandwidth and selectivity are not constant with the tuning. The noise figure is 7 dB. The compression curves for single-tone and two-tone excitations are shown in Figure 53 for both the active filter and a passive filter with the same layout but with the active elements isolated in such a way that the contributions of the varactors and of the transistors are separated. The active filter has the compression point at −1 dBm and a third-order intercept point at 12 dBm.

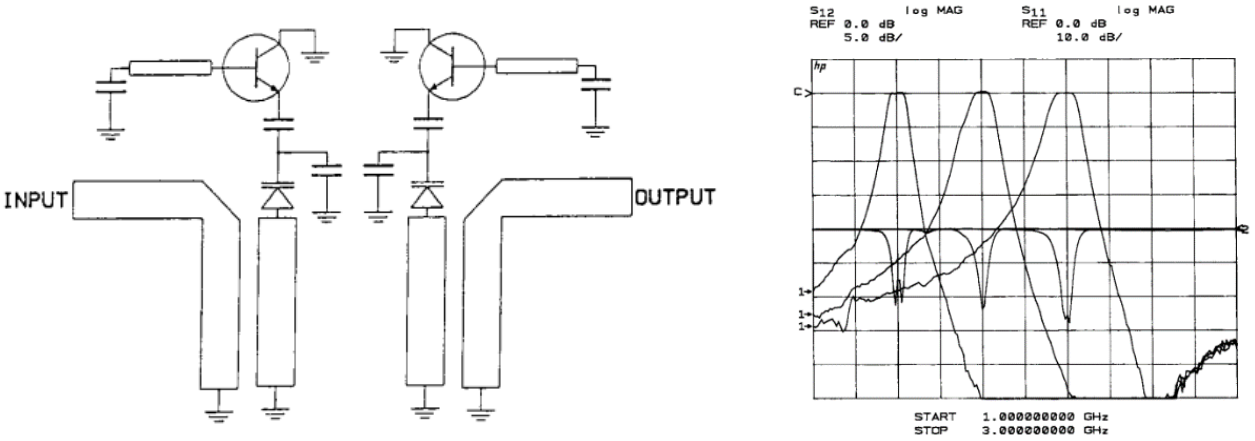

(**a**) (**b**)

Figure 52. The layout (**a**) and the S-parameters (**b**) of the filter from [21]. Reproduced with permission from [21].

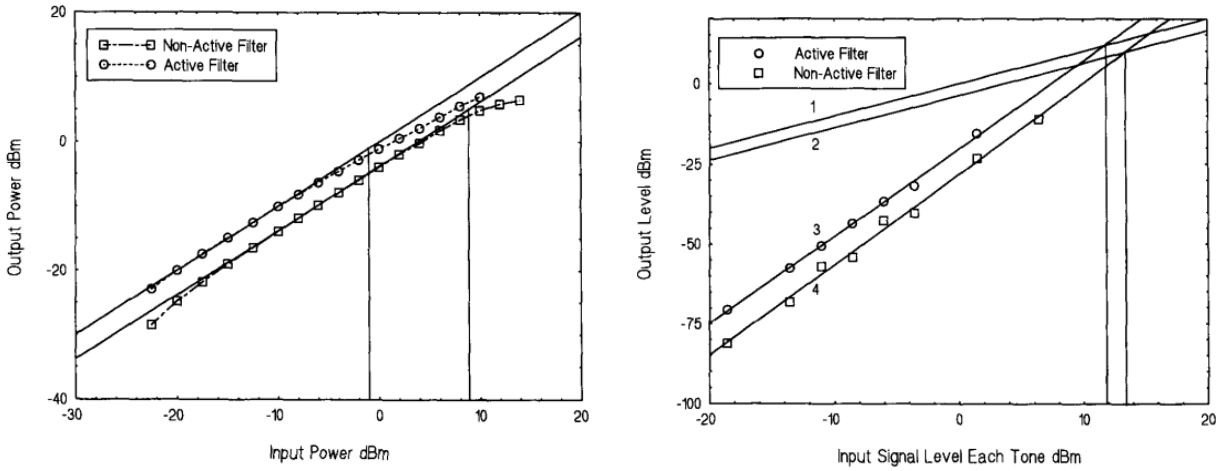

Figure 53. The single-tone compression curve (**a**) and the two-tone compression curve (**b**) of the active and passive filters from [21]. Reproduced with permission from [21].

The third example is a 20 GHz varactor-tuned MMIC filter presented in 2005 [22]. The structure of the filter is shown in Figure 54a, where the radial stubs must be replaced with varactors for the tunable version. The schematic of the negative resistance (Figure 54b) is a common-gate transistor that presents an almost constant reactive part, and a negative resistance in the band of interest. A photograph of the chip and the simulated and measured S-parameters are shown in Figure 55. The selectivity and tunability (17.5–21.5 GHz) are very good, but the passband flatness is poor (approximately 6 dB), and the gain variation with tuning is very large (from −11 to few dB). The noise figure is 17.5 dB and the compression point is −20 dBm.

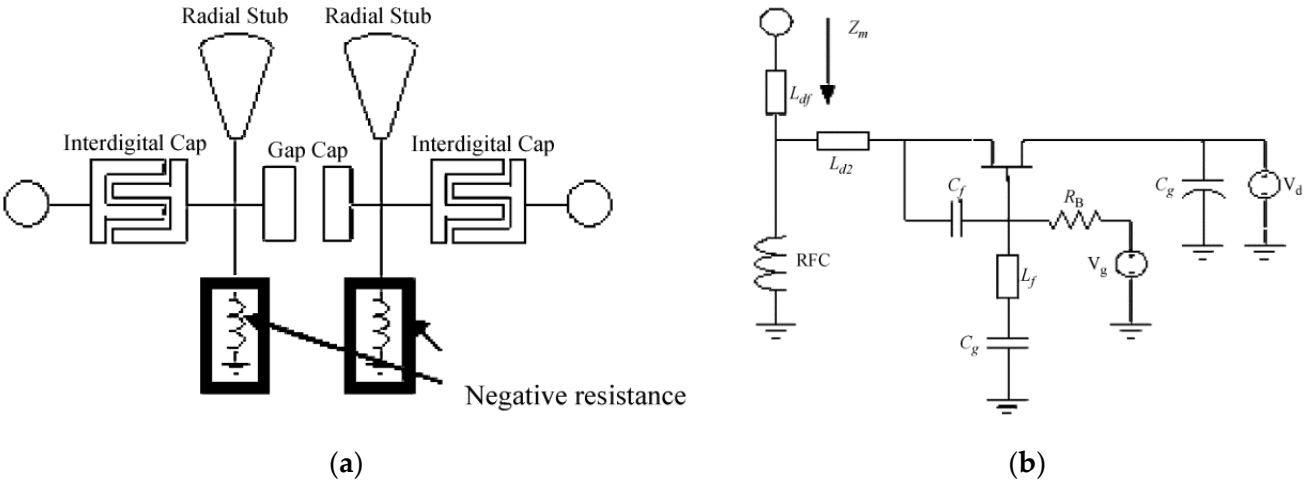

Figure 54. The structure of the filter (**a**) and the schematic of the negative-resistance component (**b**) from [22]. Reproduced with permission from [22].

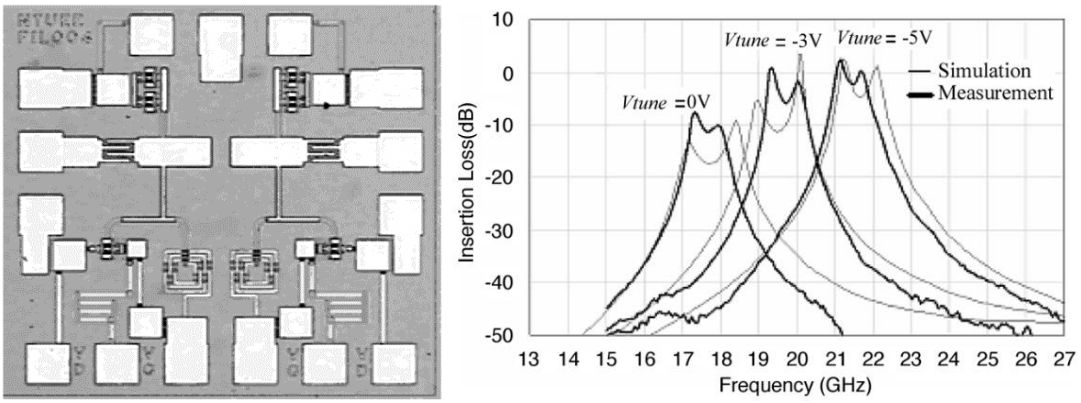

(**a**) (**b**)

Figure 55. Chip photograph (**a**) and measured and simulated S-parameters (**b**) of the tunable filter from [22]. Reproduced with permission from [22].

The last two examples have been presented by the same group in 2016 and 2017 within two versions of a dual-mode dual-conversion receiver [23,24]. The first version is implemented in 0.18 µm CMOS technology, while the second one is implemented in 0.18 µm BiCMOS technology. The receiver is a complex system, including a tunable filter with 10–20 MHz bandwidth at 5 GHz for channel selection. The filter follows a low-noise amplifier for noise figure reduction.

The schematic of the CMOS filter is shown in Figure 56 together with the chip photograph of the complete receiver. The filter is a varactor-tuned shunt LC resonator, with the transistor M6 providing the negative resistance. The voltage V_T tunes the varactors, and therefore the center frequency of the filter, while the voltage V_{q1} tunes the tail current of the transistor M6 and, consequently, the Q-factor of the filter. The effect of both tuning voltages separately is shown in Figure 57a, where the center frequency and the Q-factor are tuned separately. In Figure 57b, the combined tuning gives a relatively constant gain and bandwidth across the frequency tuning range. The picture actually represents the conversion gain of the complete receiver, therefore including not only the LNA upstream but also the Gilbert-cell mixer with output buffer downstream. The total noise figure is 9 dB, and the compression point is −50 dBm. Figure 57b shows the performances of three different chips, illustrating the dispersion due to fabrication tolerances.

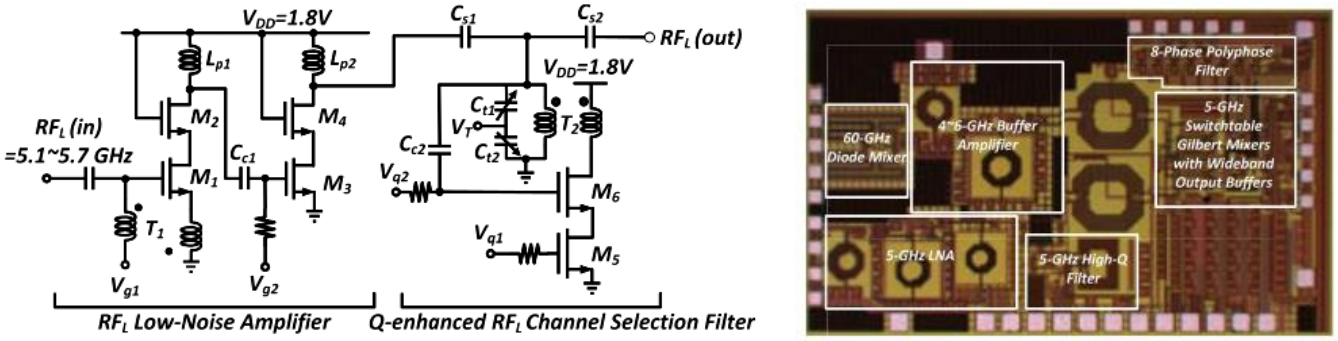

(**a**) (**b**)

Figure 56. The schematic of the LNA and of the filter (**a**) and the chip photograph (**b**) from [23]. Reproduced with permission from [23].

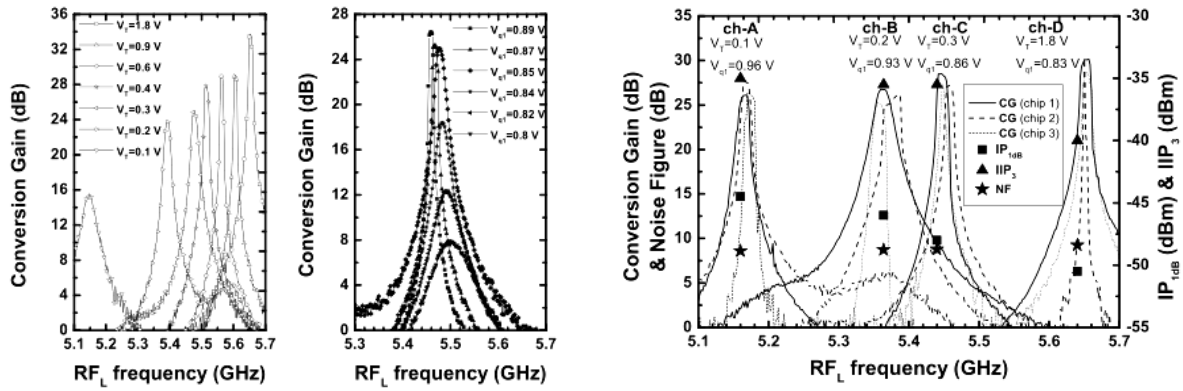

(**a**) (**b**)

Figure 57. Conversion gain for independent tuning (**a**) and conversion gain for combined tuning for three chips and four channels (**b**) from [23]. Reproduced with permission from [23].

The schematic of the BiCMOS filter is shown in Figure 58 together with the chip photograph of the complete receiver. The filter is a varactor-tuned shunt LC resonator, with the cross-coupled transistor pair providing the negative resistance. The voltage V_T tunes the varactors and therefore the center frequency of the filter, while the voltage V_q tunes the tail current of the transistors and consequently the Q-factor of the filter. Figure 59 shows the conversion gain of the whole receiver for the two extreme channels.

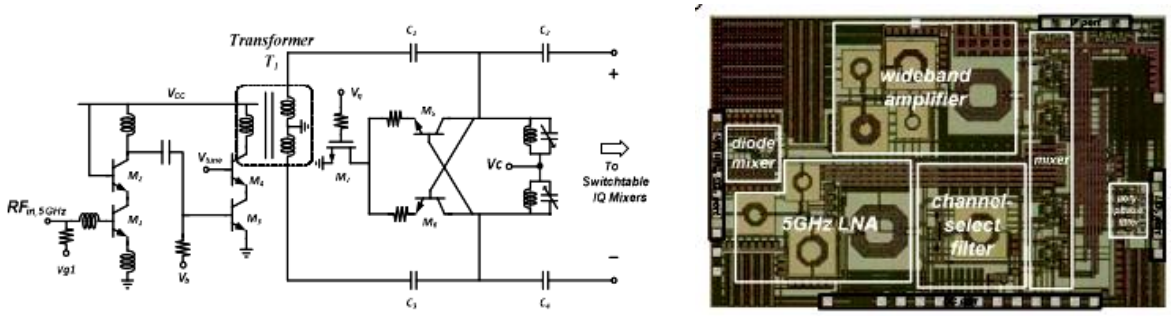

(**a**) (**b**)

Figure 58. The schematic of the LNA and of the filter (**a**) and the chip photograph (**b**) from [24]. Reproduced with permission from [24].

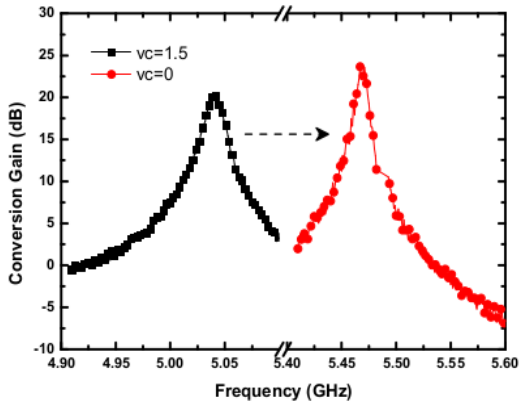

Figure 59. Conversion gain of the receiver for two extreme channels from [24]. Reproduced with permission from [24].

Overall, negative-resistance tunable filters are a promising approach in terms of the tunability, passband flatness, selectivity, and compression point. The noise figure tends to be high, especially in the monolithic implementations, where the negative resistance must have a high value in order to compensate for the high losses of the passive elements. A drawback is due to the fact that the tunability is obtained only through varactors.

3.2. Active Inductance Filters

Only a few filters based on active inductors have been published, and most of them more than 15 years ago, with no consequences. The active inductor has a negative resistive part that compensates for the losses of the passive elements, but also generates noise. The potential tunability of the inductive part is its main advantage over pure negative-resistance components. We will describe fixed-frequency filters first, and then tunable ones.

A fixed-frequency MMIC filter from 1993 has been published in [3], fabricated by the GEC-Marconi (Caswell) F20 foundry process. The schematic and the chip photograph of the active inductor are shown in Figure 60, and the reflection coefficient is plotted in Figure 61a, indicating almost zero losses at the center frequency of the filter. The structure of the complete three-cell filter is shown in Figure 61, and the measured and simulated transfer function are shown in Figure 61b. The filter (Figure 62) has low losses, excellent selectivity, and a reasonable passband flatness. Nothing is said about the noise figure or compression point.

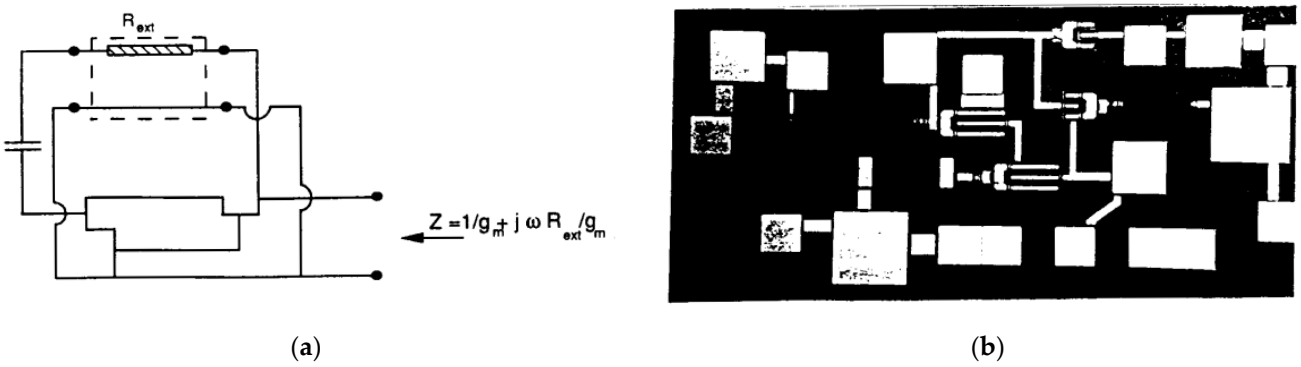

(**a**) (**b**)

Figure 60. The schematic of the active inductor (**a**) and the chip photograph (**b**) from [3]. Reproduced with permission from [3].

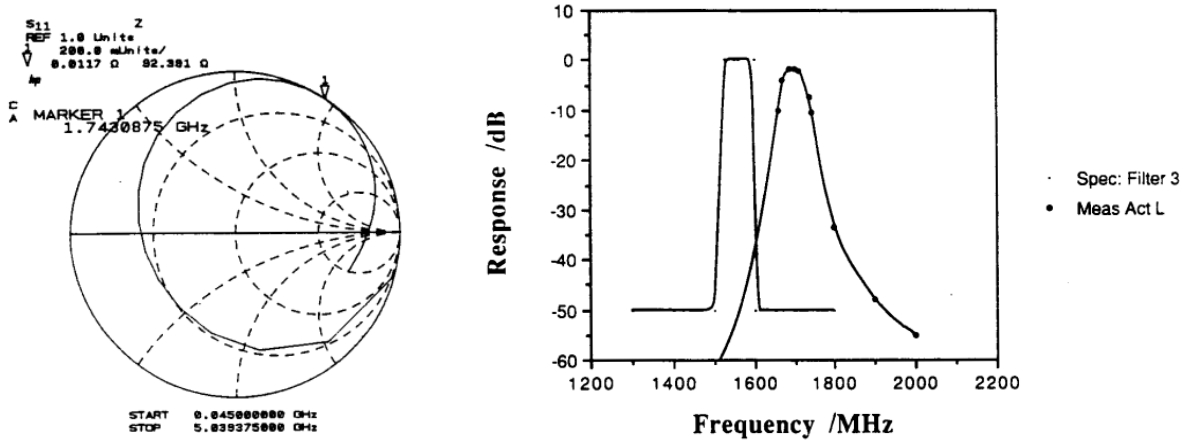

(**a**) (**b**)

Figure 61. The input reflection coefficient of the active inductor (**a**) and the simulated and measured transfer function of the filter (**b**) from [3]. Reproduced with permission from [3].

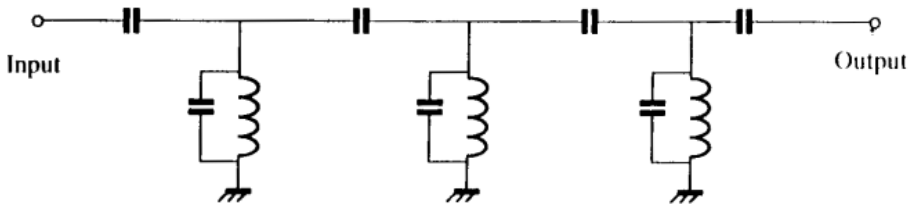

Figure 62. The schematic of the filter based on active inductors from [3]. Reproduced with permission from [3].

Another fixed-frequency filter at 22 GHz based on active inductors has been published in 2001 in [25], realized with the ED02AH process from the PML foundry. The schematic of the resonant cell, including the shunt capacitor and the active inductor, is shown in Figure 63, together with a photograph of the complete filter, which is composed of two shunt resonant cells and an amplifier. The measured S-parameters show excellent selectivity, a very good match, and an extremely low noise figure (Figure 64). No explanation is given for the very low value and shape of the noise figure, and no information on the compression point is available.

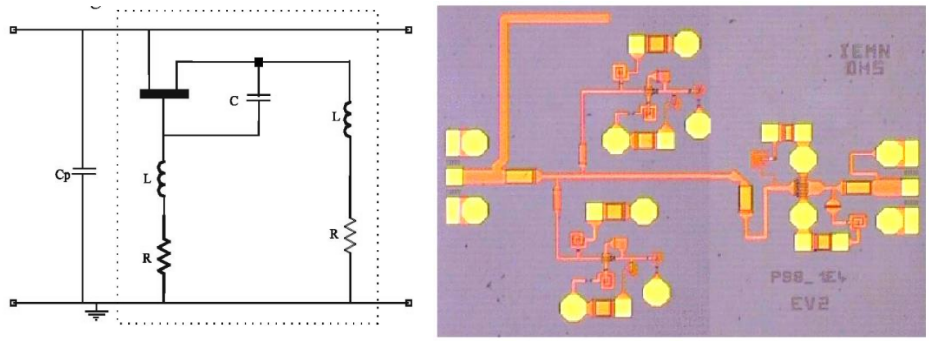

(**a**) (**b**)

Figure 63. The schematic of the resonant cell including the active inductor (**a**) and the chip photograph of the complete filter (**b**) from [25]. Reproduced with permission from [25].

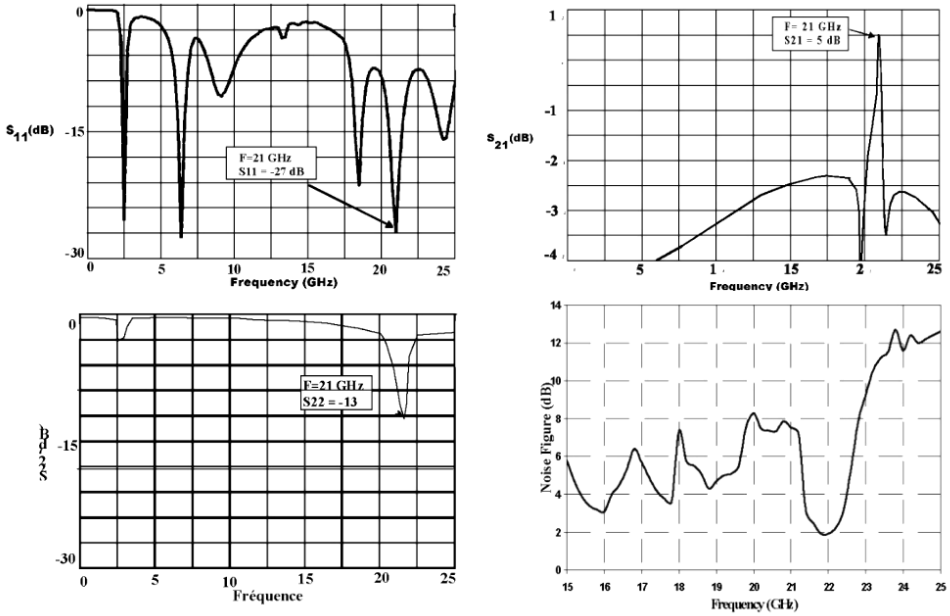

Figure 64. The measured S-parameters and the noise figure of the filter from [25]. Reproduced with permission from [25].

Not many tunable filters based on active inductors have been presented. The first example from 1994 in MMIC technology uses only varactors for tuning [26], and it was realized from Ferdinand-Braun-Institut für Höchstfrequenztechnik Berlin. The simplified schematic of both the active inductor with its equivalent circuit and of the complete filter are shown in Figure 65. The equivalent negative resistance and inductance of the active inductor are shown in Figure 66, together with the schematic of the tunable filter. The measured S-parameters are shown in Figure 67. The filter has good tunability (200 MHz) and selectivity, but a poor input match (−5 dB) and a high gain variation when tuned (−5 dB). The compression point of a fixed-frequency version of the filter has a compression point of −7 dBm; the compression of the tunable version has not been measured and should be a few dB worse. No information is given on the noise figure.

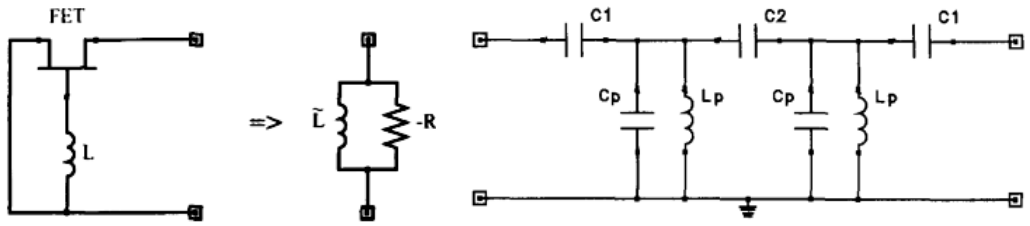

(**a**) (**b**)

Figure 65. The simplified schematic of the active inductor (**a**) and of the complete filter (**b**) from [26]. Reproduced with permission from [26].

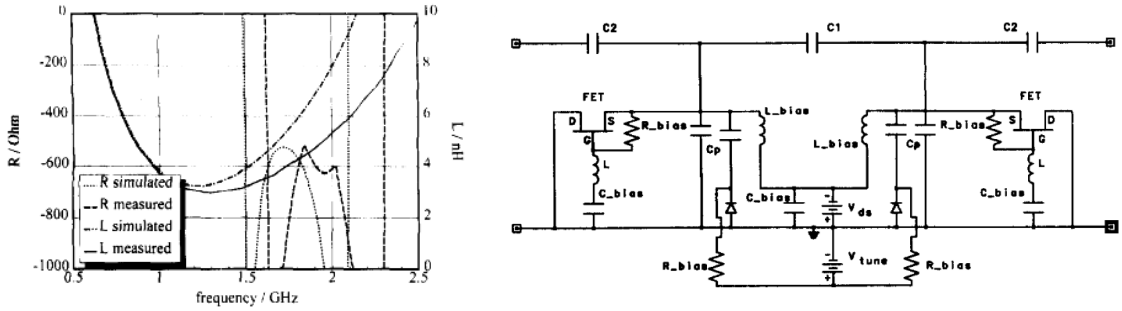

(**a**) (**b**)

Figure 66. The equivalent negative resistance and inductance of the active inductor (**a**) and the schematic complete filter (**b**) from [26]. Reproduced with permission from [26].

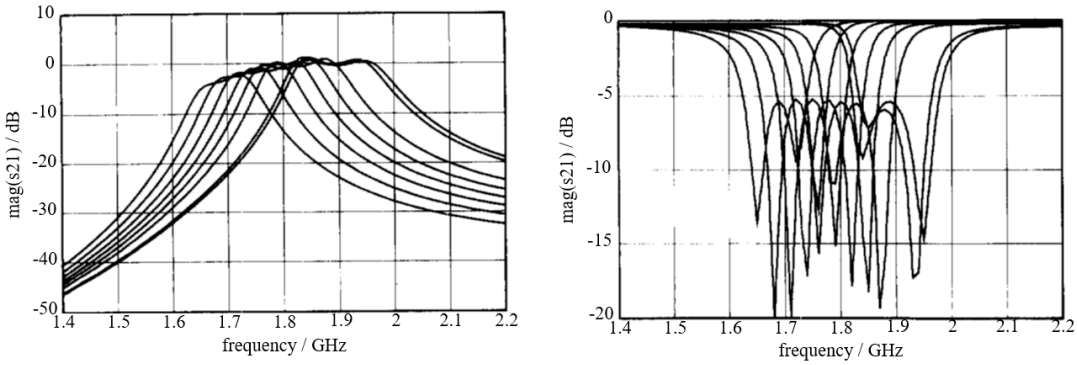

(**a**) (**b**)

Figure 67. The measured S-parameters of the complete filter from [26]: S21 (**a**) and S11 (**b**). Reproduced with permission from [26].

The second example at 15 GHz in MMIC technology, from 2005, uses the tuning of both the resistive and reactive parts of the active inductor for the frequency and gain tuning of the filter [27]. The structure of the filter is shown in Figure 68, together with the simplified schematic of the active inductor. The passive section of the filter is a half-wavelength resonator coupled to the input and output ports. The active inductor is added in the middle point (at point A), for the tuning of the resonating frequency and of the losses of the resonator. The reactive part of the active inductor is tuned by means of the series varactor, while the resistive part is controlled by the transistor bias. The impedance of the active inductor is shown in Figure 69, together with the measured S-parameters. The filter is basically a single-cell structure and therefore the passband flatness is very poor. However, the tunability, selectivity and gain uniformity across the tuning band are very good. No information is given on the noise figure and compression point.

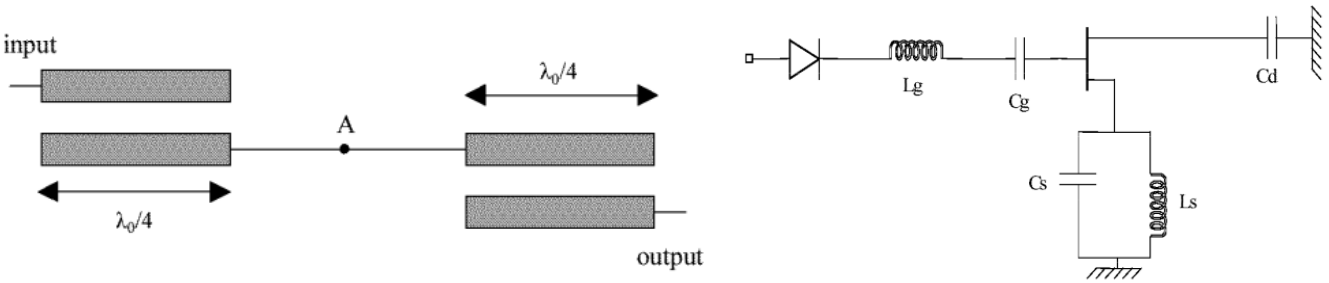

(**a**) (**b**)

Figure 68. The structure of the filter (**a**) and the simplified schematic of the active inductor (**b**) from [27]. Reproduced with permission from [27].

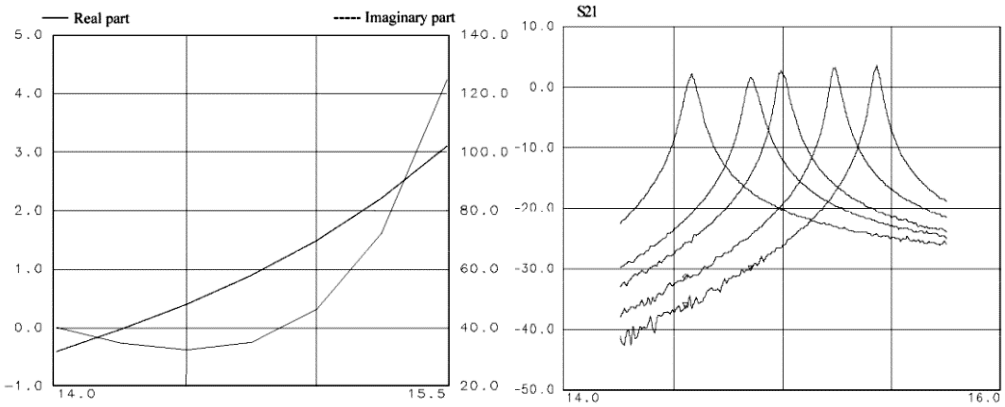

(**a**) (**b**)

Figure 69. The equivalent negative resistance and inductance of the active inductor (**a**) and the measured S-parameters of the filter (**b**) from [27]. Reproduced with permission from [27].

A tunable filter at 2.3 GHz in 0.18 µm BiCMOS technology has been presented in 1997 in [28]. The filter is based on an active inductor with a gyrator structure and a three-cell topology shown in Figure 70.

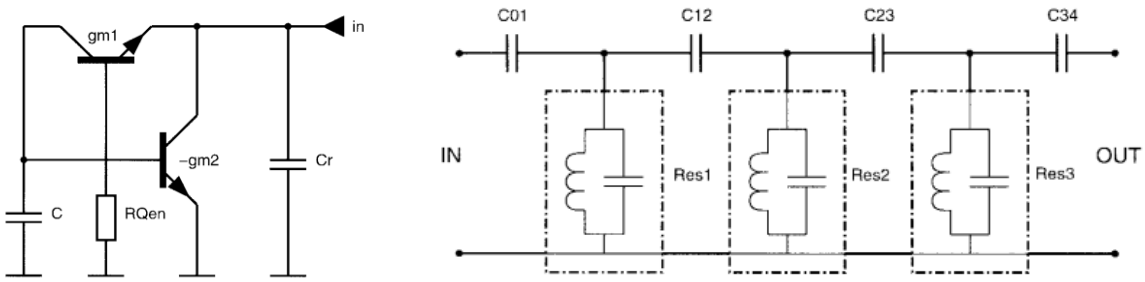

(**a**) (**b**)

Figure 70. The structure of the resonator with the active inductor (**a**) and of the filter (**b**) from [28]. Reproduced with permission from [28].

The actual schematic of the active inductor is shown in Figure 71 together with a photograph of the chip. The two bias voltages of the active inductor allow for the almost independent tuning of the inductive and resistive parts, controlling the center frequency of the filter and the Q-factor of the inductance, and therefore the gain of the filter. The measured transfer function of the filter is shown in Figure 72. The tunability and gain uniformity are very good, as well as selectivity. However, the passband is strongly distorted at the extremes, mainly because the three cells share the same bias voltages, whereas independent tuning would give much better results. The compression point is −20 dBm and the noise figure is 35 dB, which is quite high.

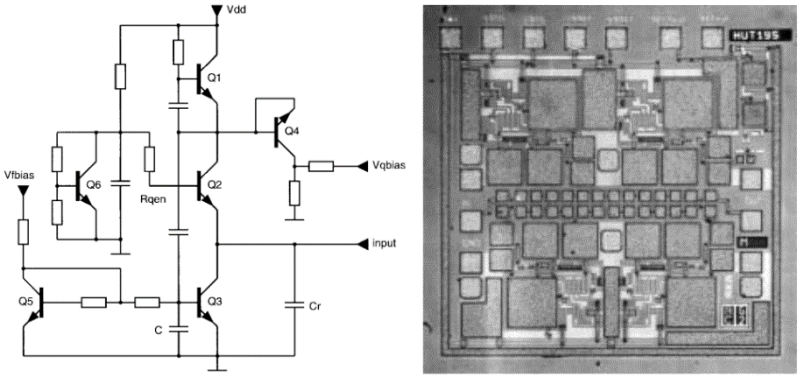

(**a**) (**b**)

Figure 71. The schematic of the resonator with the active inductor (**a**) and a chip photograph (**b**) from [28]. Reproduced with permission from [28].

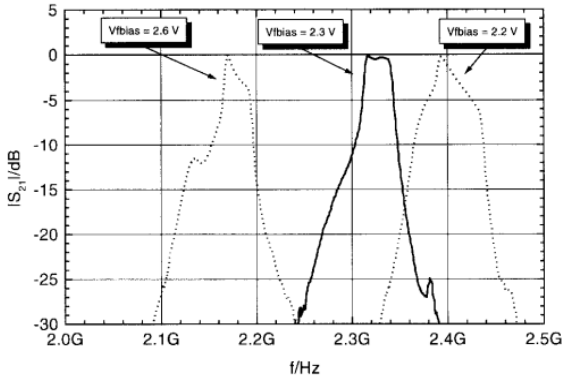

Figure 72. The measured transfer function of the filter from [28]. Reproduced with permission from [28].

A 5.7 GHz tunable filter in 0.18 µm CMOS technology has been presented in [29] in 2004. The simplified and detailed schematics of the active inductor, based on the gyrator approach, are shown in Figure 73. The non-inverting transconductance is implemented with an unbalanced differential pair M1–M2, and the inverting transconductance with a common-source amplifier M3. The complete schematic includes two tuning voltages for the almost independent setting of the inductance value and of the negative resistance value, and therefore of the center frequency and of the gain of the filter, respectively.

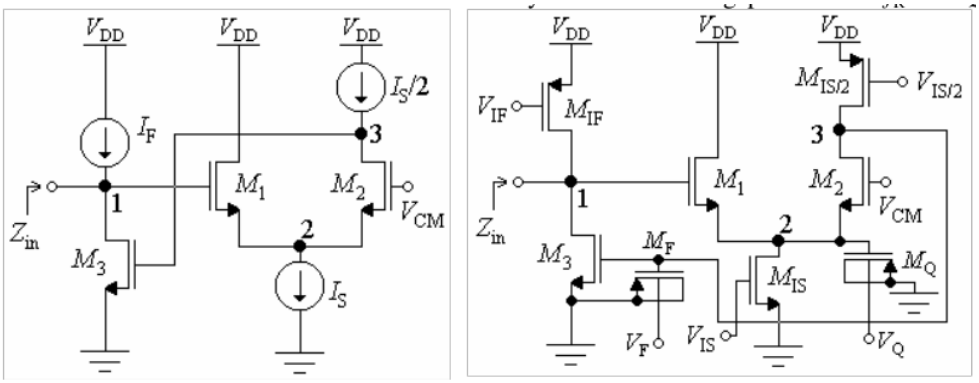

(**a**) (**b**)

Figure 73. The simplified (**a**) and detailed schematics (**b**) of the active inductor from [29]. Reproduced with permission from [29].

The structure of the complete filter is shown in Figure 74 together with the measured S-parameters at the central tuning frequency. The transconductance M1 at the input of the filter converts the input voltage into current, which is fed to the active inductor. The voltage drop across the inductor is transferred to the load by means of a buffer M_{out}. Selectivity of the filter is very good, and the tuning range is excellent (Figure 75). However, the noise figure is 35 dB and the compression point is −30 dBm, making the filter difficult to use in practical conditions.

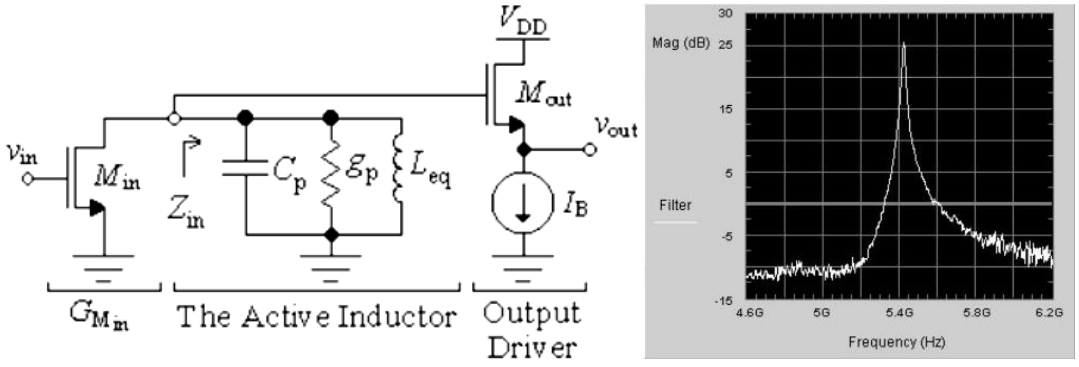

(**a**) (**b**)

Figure 74. The structure of the complete filter (**a**) and the measured transfer function (**b**) of the complete filter from [29]. Reproduced with permission from [29].

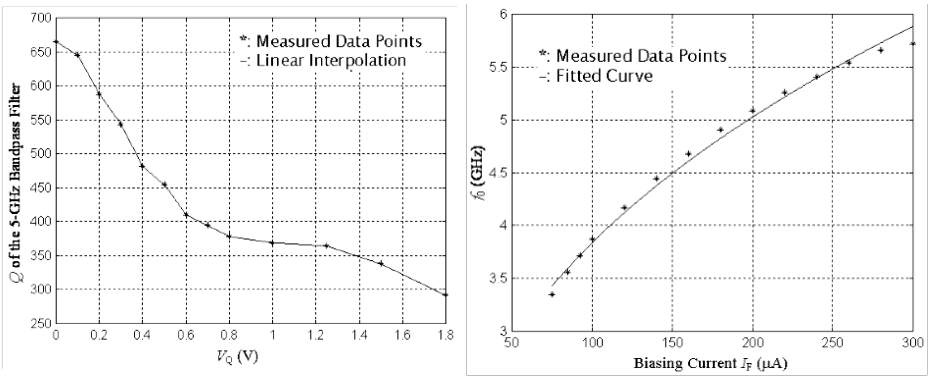

(**a**) (**b**)

Figure 75. Q-factor (**a**) and frequency (**b**) tuning of the filter from [29]. Reproduced with permission from [29].

Another filter in 0.18 μm CMOS technology at 2.4 GHz has been presented in [30] in 2018. The filter is based on a stepped-impedance ring resonator with four high-Q active inductors. The active inductor has a gyrator structure (Figure 76). The schematic of the ring is shown in Figure 77 together with the complete filter structure, which includes an LNA at the input for noise figure reduction.

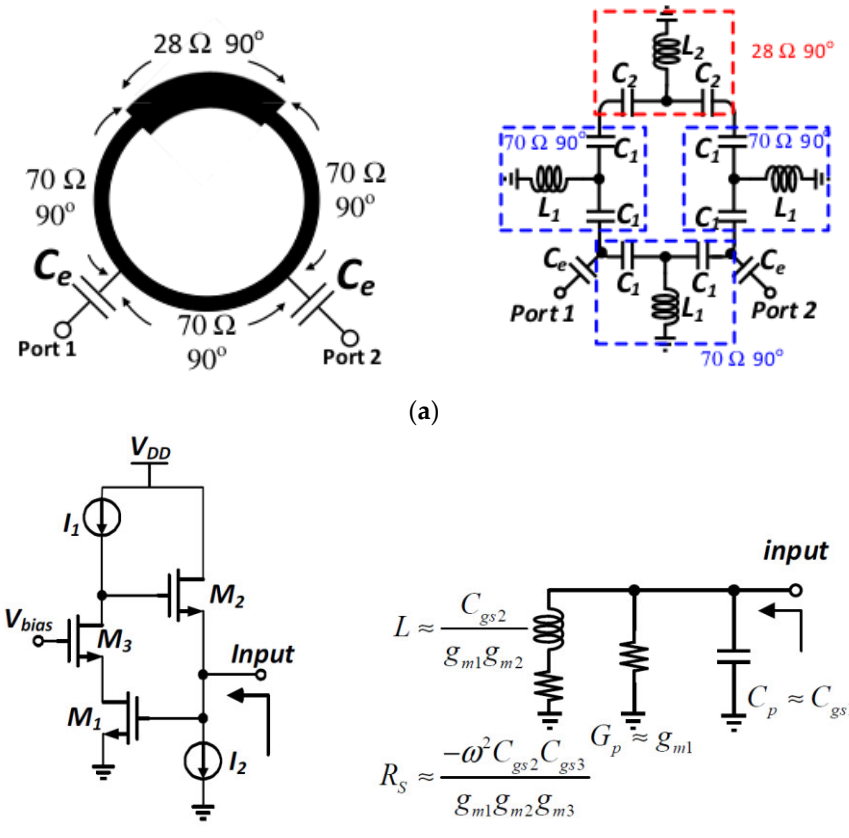

(**a**)

(**b**)

Figure 76. Filter (**a**) and active inductor (**b**) structures from [30]. Reproduced with permission from [30].

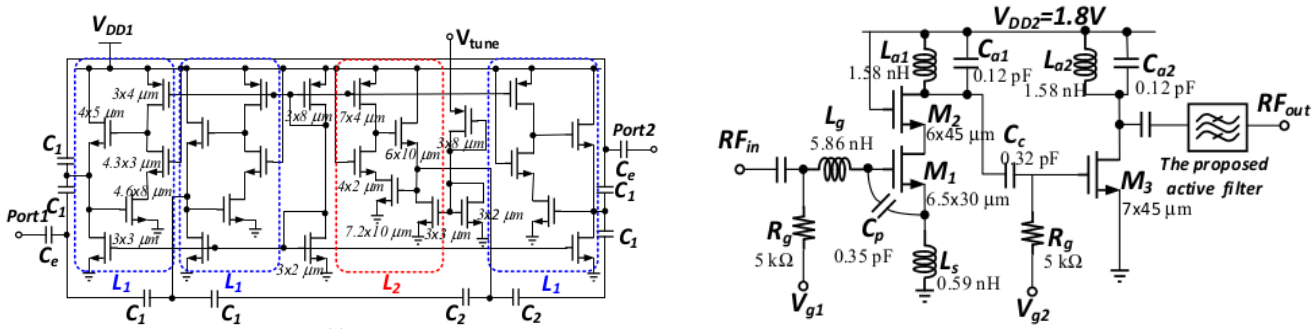

(**a**) (**b**)

Figure 77. Schematic of the ring (**a**) and of the complete filter (**b**) from [30]. Reproduced with permission from [30].

The S-parameters of the filter are shown in Figure 78 for a fixed frequency, but with bandwidth tuning through the control of the Q-factor of the inductor. The frequency tuning of the filter is also shown in the same figure. The tuning range is very wide; selectivity and matching are good, at least toward the low frequencies. The noise figure of the filter alone is 24 dB, which drops to 8 dB when including the input LNA. The compression point of the filter is −34 dBm, which becomes −54 dBm when including the LNA (Figure 79).

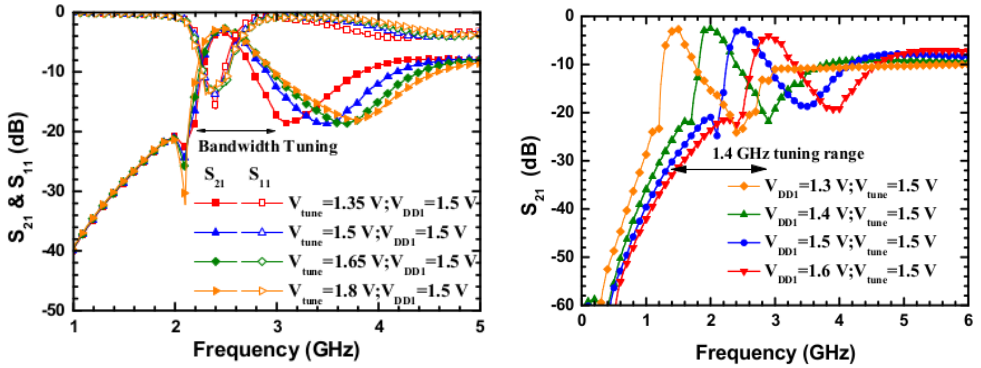

(**a**) (**b**)

Figure 78. Bandwidth (**a**) and center frequency tuning (**b**) from [30]. Reproduced with permission from [30].

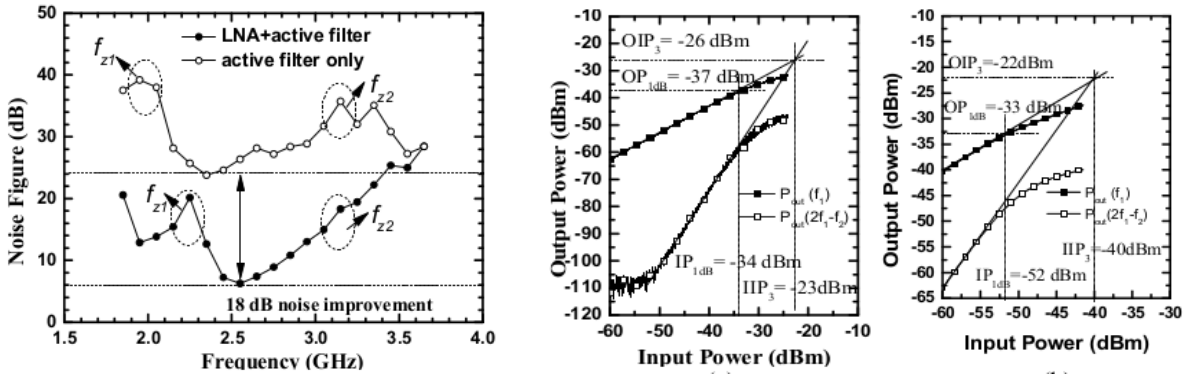

(**a**) (**b**)

Figure 79. Noise figure (**a**) and compression curves (**b**) of the filter, with and without the input LNA, from [30]. Reproduced with permission from [30].

In addition, some of the same authors have worked a lot in the last few years on the definition of tunable active filters based on an active inductor [31–40]. Its main feature is the simplicity of the topology, requiring only one transistor per cell, with a fixed bias. The tunability is obtained by means of varactors. As a result, stability, tunability, and dynamic range are greatly improved compared to other implementations. The areas of potential improvement are the power consumption and noise, where performances will never be as good as in passive implementations, but where some steps forward are still desirable. Most examples so far have been realized with hybrid implementations [32,37]. However, integrated solutions have also been fabricated and demonstrate the feasibility of the monolithic approach [31,34,35]. The basic topology of the conceived filter is shown in Figure 80. A single cell is a shunt-resonating LC cell. The variable capacitor is implemented with a varactor. The tunable inductor is an active inductor, as described below. The coupling may be capacitive, inductive, or LC-series. A possible implementation of the active inductor is shown in Figure 81. The input voltage is attenuated and delayed by the phase-shifting network, then fed to the active device (either a FET or a transistor) in an inverting configuration, which is typically a Common Emitter or Common Source. The 180° phase inversion turns the current from capacitive to inductive with respect to the input voltage. Therefore, the network simulates an inductor. The tunability is obtained with the presence of one or two varactors within the phase-shifting network. An alternative implementation is shown in Figure 82. The main element of the inductor is an LC-series, above resonance, that behaves as a variable inductance if the capacitance is a varactor. The input voltage is sampled by a transistor whose current is fed back through a phase-shifting network. The phase and amplitude of the current of the transistor is adjusted in such a way that it compensates for the losses in the main inductive branch. This alternative implementation ensures a lower power consumption, and is currently preferred.

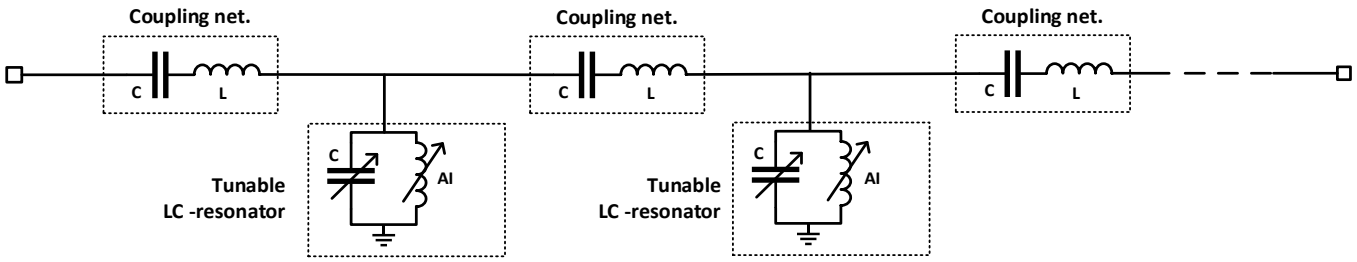

Figure 80. Basic topology of the filter.

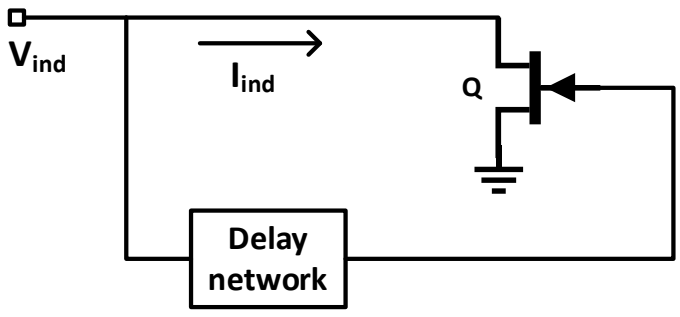

Figure 81. A possible implementation of the active inductor.

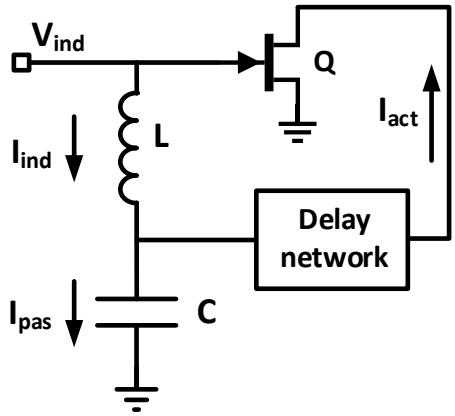

Figure 82. An alternative implementation of the active inductor.

Among different solutions [31–40], it is important to cite the one analyzed in [31,34]. A monolithic two-cell filter has been designed and fabricated at 2 GHz with p-HEMT technology from HSRI. Since the varactors are under development and not yet available in this technology, three separate filters with fixed capacitances have been fabricated, centered at three different frequencies. The tuning capacitors have values compatible with the varactors under development, and will be implemented as such, as soon as the technology is available.

The filters have a bandwidth of 30 MHz and can potentially be tuned between 1.8 GHz and 2.1 GHz. The measured S-parameters of the three filters are shown in Figure 83. The dynamic range is approximately 75 dB with a 1 dB compression at −7 dBm. The chip has a 3 mm × 1.5 mm area and a power consumption of 120 mW at 4 V supply voltage. The layout of the chip is shown in Figure 84.

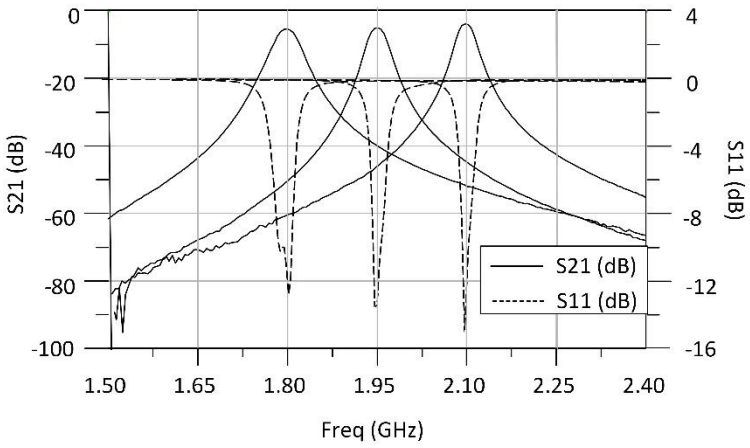

Figure 83. Measured S-parameters of the two-cell monolithic filters, from [34]. Reproduced with permission from [34].

Overall, the GaAs versions of the filters based on active inductors show good tunability and very good selectivity, but require accurate tuning. The SiGe and CMOS versions have excellent tunability, but a very high noise and a very low compression point, perhaps because of the low-power approach of the published filters.

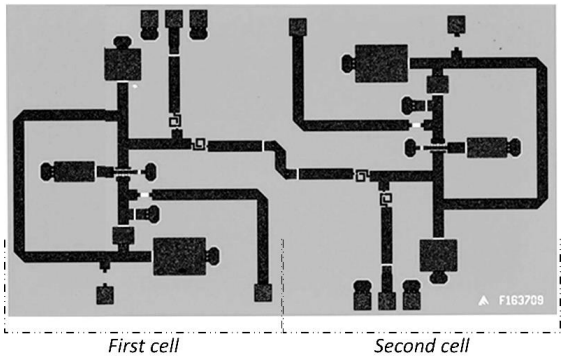

Figure 84. Layout of the two-cell monolithic filter, from [34]. Reproduced with permission from [34].

3.3. Active Negative Capacitance Filters

A further solution among the negative resistance solutions consists in the use of a resonator realized with a conventional inductance and an active negative capacitor realized, for instance, with a FET transistor that exhibits negative capacitance and resistance. In this way, the active device is able to compensate for the loss introduced by the passive inductor. For the sake of illustration, an interesting example is reported in [41]; the filter has not been fabricated and the analysis has been carried out only at simulation level. The simplified schematic of the active negative capacitance is reported in (Figure 85a), where two Fujitsu FSX017X GaAs FETs have been used, while the second order complete filter is shown in Figure 85b. The center frequency of the filter is 1.3 GHz (Figure 86a) with a −3 dB bandwidth of 640 MHz. The rejection is not so high, showing −10 dB at 1 GHz from the central frequency. Finally, the noise figure is 2.5 dB (Figure 86b).

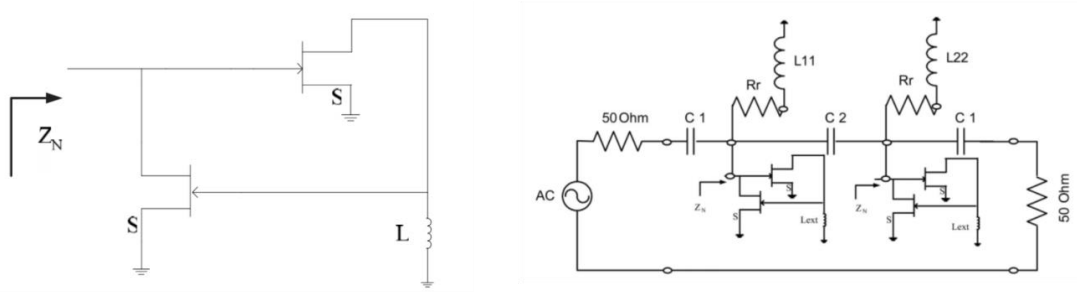

(**a**) (**b**)

Figure 85. Schematic of the active negative capacitance (**a**) and of the complete filter (**b**) proposed in [41]. Reproduced with permission from [41].

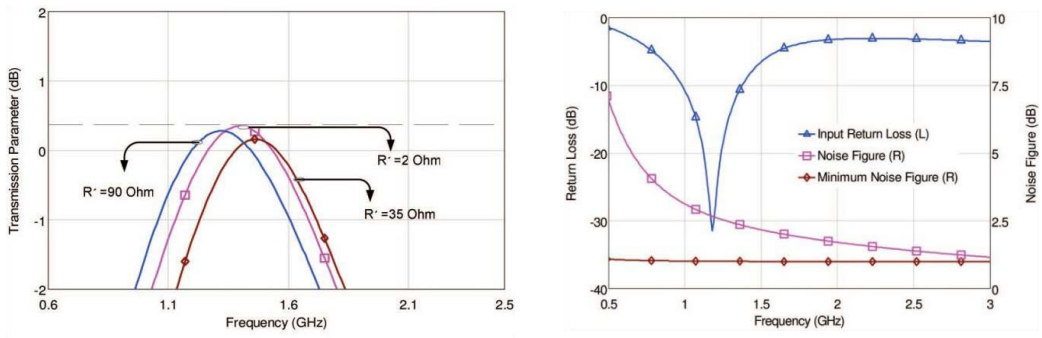

(**a**) (**b**)

Figure 86. Transfer function for different values of the resonator resistance (**a**) and return loss and noise of the complete filter (**b**) proposed in [41]. Reproduced with permission from [41].

4. Filters Based on the Use of Switches and Capacitors

These kinds of filters have been defined with several names in the past, as filters using modulation, filters using commutated capacitors, sampled-data filters, and N-path filters [42]. Basically, a N-path filter is realized with an array (N size) of commutated capacitors driven with different phases of a clock that determines the resonant frequency (Figure 87); this structure allows a transfer function to be obtained that is similar to those achievable with a high-Q second-order RLC resonator [43]. The 3 dB bandwidth of a N-path filter is determined by the number N and by RC product: $BW_{-3dB} = 1/\pi NRC$, which means it is inversely proportional to the total capacitance N·C. In the Figure 88 example, the input signal is coherent with the clock frequency and the output signal (V_{out}) is a sampled and held version of the input one (V_{in}). Additionally, if the V_{in} frequency is not strictly coherent, the mean voltage value stored in the capacitors for a long period of integration is 0. This simple assumption should explain why this kind of filter shows a very high selectivity.

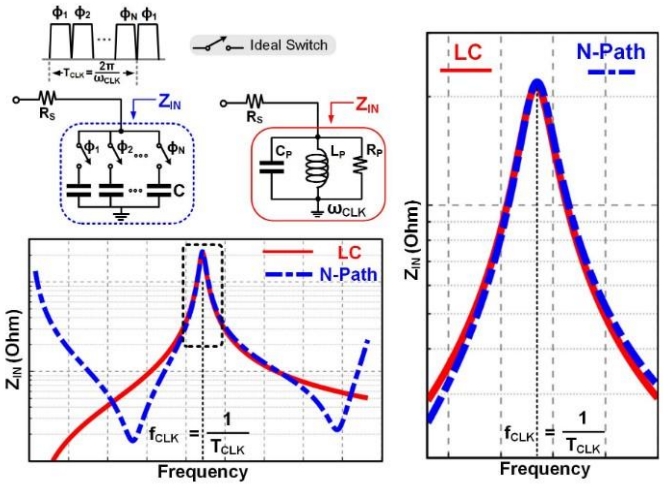

Figure 87. Transfer function of a N-path filter and its equivalent LC version [43]. Reproduced with permission from [43].

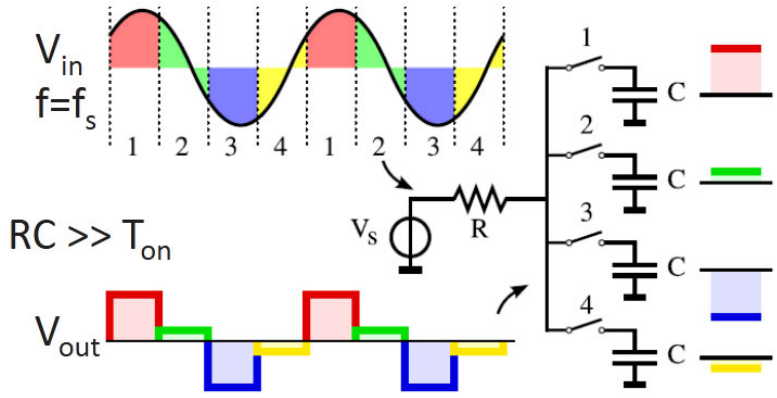

Figure 88. Time-domain waveforms with 4-path switch-R-C filter [42]. Reproduced with permission from [43].

The architecture of N-path filters makes them particularly suitable for CMOS integration and software radio applications. A valuable review of this kind of filter has been carried out in [42], in which several aspects have been investigated, such as power consumption, linearity, noise performance, and future applications. As general considerations, N-path filters have a controllable gain and linearity comes at the expense of noise performance. Linearity is mainly determined by the linearity of the active devices (CMOS) used

as switches, which depends on the voltage swing and input frequency. Tunability can also be achieved properly by choosing a clock frequency and capacitor values. This kind of filter has the perspective to replace saw filters in modern reconfigurable RF transceivers, even if, up to now, the main solutions that have been proposed in the literature have operation frequencies limited to a few GHz. Good operations at higher frequencies, where parasitics strongly increase, have not yet been demonstrated, and it is yet to be proven whether this type of filter is useful in practical applications in terms of its shape factor, i.e., in-band ripple and out-of-band selectivity.

An interesting solution has been proposed in [43]. It is realized in a 65 nm CMOS technology and covers the bandwidth 0.8–1.1 GHz. In Figure 89a, the complete schematic of the adopted solution is reported, while in Figure 89b, a microchip photo is shown. The filter can be tuned a bit in terms of both the bandwidth and center frequencies, and the results are reported in Figure 90. The 3 dB bandwidth spans from 30 to 50 MHz, while the insertion loss is in the range $-4.6 \div -3.8$ dB and the noise figure is between 5 and 8.6 dB. Regarding linearity, the in-band 1 dB compression point is approximately 7 dBm.

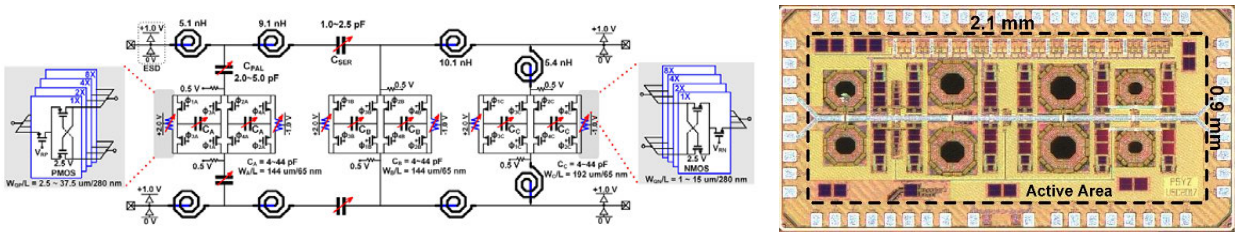

(**a**) (**b**)

Figure 89. N-path filter proposed in [43]. Schematic (**a**) and chip photo (**b**) of the filter prototype. Reproduced with permission from [43].

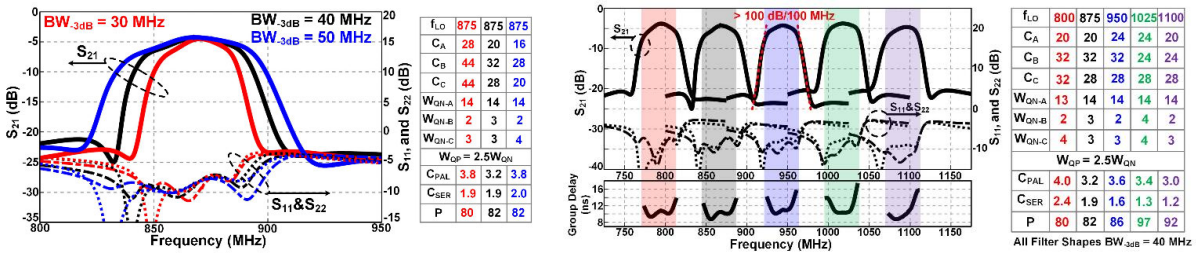

f_{LO}	875	875	875
C_A	28	20	16
C_B	44	32	28
C_C	44	28	20
$W_{QN\text{-}A}$	14	14	14
$W_{QN\text{-}B}$	2	3	2
$W_{QN\text{-}C}$	3	3	4
$W_{QP} = 2.5W_{QN}$			
C_{PAL}	3.8	3.2	3.8
C_{SER}	1.9	1.9	2.0
P	80	82	82

f_{LO}	800	875	950	1025	1100
C_A	20	20	24	24	20
C_B	32	32	32	24	24
C_C	32	28	28	28	28
$W_{QN\text{-}A}$	13	14	14	14	14
$W_{QN\text{-}B}$	2	3	2	4	2
$W_{QN\text{-}C}$	4	3	3	4	3
$W_{QP} = 2.5W_{QN}$					
C_{PAL}	4.0	3.2	3.6	3.4	3.0
C_{SER}	2.4	1.9	1.6	1.3	1.2
P	80	82	86	97	92

(**a**) (**b**)

Figure 90. (**a**) Measured filter shape for different bandwidths; (**b**) S-parameters and group delay of the filter centered at different frequencies [43]. Reproduced with permission from [43].

A further solution based on N-path architecture is proposed in [44], where the filter is coupled with an LNA for channel selection in cellular systems. The proposed circuit operates from 0.4 to 6 GHz and it is realized with 32 nm CMOS SOI. Figure 91a illustrates the complete schematic, while in Figure 91b the correspondent layout is reported. The hybrid N-path filter is useful for suppressing the TX leakage and improves linearity with the sideband rejection. In Figure 92a, the measured S21 and S11 are reported in the full tuning range. It is evident that both the gain and out-of-band rejection decrease for higher frequencies, which is due to the clock and duty cycle distortion when the center frequency increases. The 3 dB bandwidth is 15 MHz and the roll-off slope is approximately 30 dB/100 MHz. The noise figure is reported in Figure 92b and it shows a variation of approximately 1.5 dB in the full tuning bandwidth. The 1 dB compression point is approximately 0 dBm.

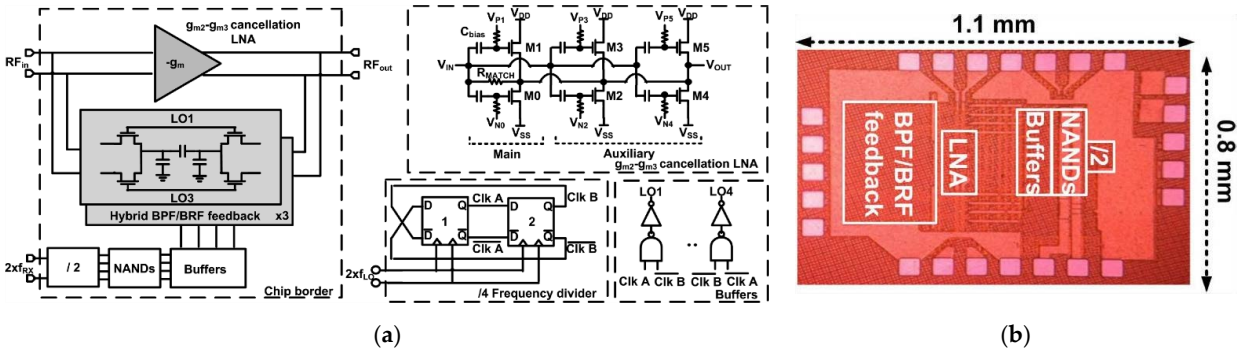

(**a**) (**b**)

Figure 91. Schematic (**a**) and chip photo (**b**) of the complete prototype proposed in [44]. Reproduced with permission from [44].

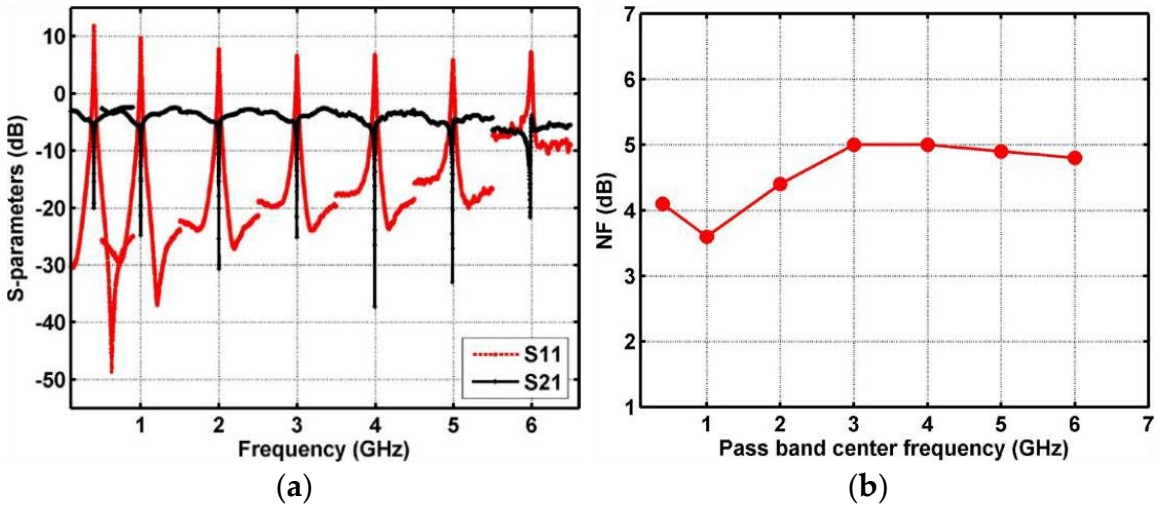

(**a**) (**b**)

Figure 92. Measured S-parameters (**a**) and noise figure (**b**) for different center frequencies [44]. Reproduced with permission from [44].

Finally, it is worth noting a tentative N-path design at a higher frequency in [45]. This bandpass filter operates in a frequency range spanning from 0.1 to 12 GHz with a constant 3 dB bandwidth of 150 MHz. This solution, realized with the IBM 32 nm SOI CMOS process, to the best of our knowledge, also provides the widest tuning ranges among the N-path filters. A two-stage filter is proposed (Figure 93a) and is driven by a 4-phase local oscillator obtained from a frequency divider. The chip is very compact and a photograph is presented in Figure 93b. Regarding the performance, the insertion loss changes from 3 to 7.4 dB in the full bandwidth and increases at higher frequencies (Figure 94a). The tunability is very wide and has a constant 3 dB bandwidth, but performance is not constant in terms of input matching. The noise performance is not provided, while the nonlinear characteristics are presented in Figure 94b. Additionally, in this case, the intercept point changes a lot in the tuning bandwidth, preventing, de facto, a real use in wideband applications. These limits are probably due to the increase in clock variation times at higher frequencies, compared to the duty cycle of the clocks.

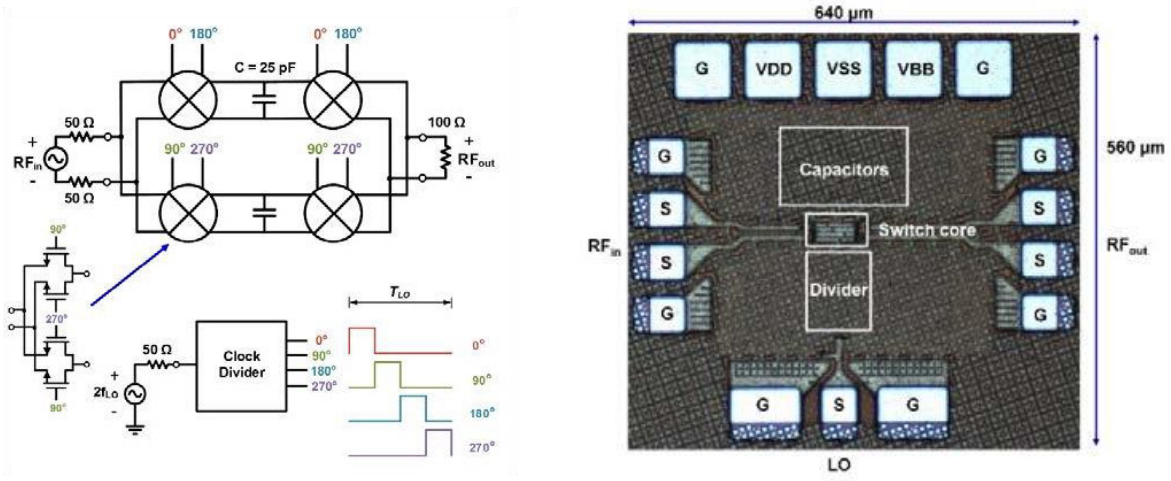

(**a**) (**b**)

Figure 93. (**a**) N-path filter architecture proposed in [45] and its chip photograph (**b**). Reproduced with permission from [45].

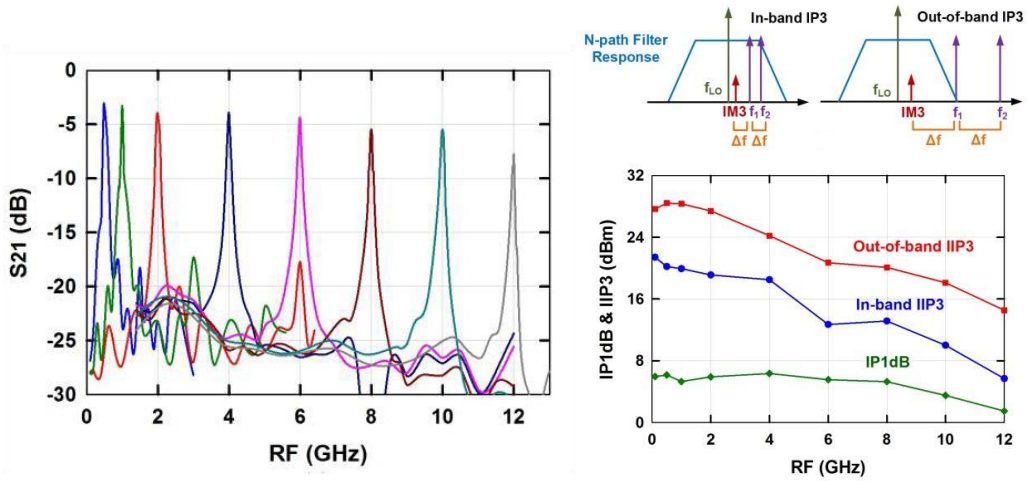

(**a**) (**b**)

Figure 94. Measured S21 (**a**) and nonlinear behavior (**b**) in the full tuning bandwidth [45]. Reproduced with permission from [45].

5. Conclusions

As stated above, a review of the state of the art of microwave active filters reveals an immature level of development but also some potentially good perspectives. The main advantages of active filters are the high selectivity even at high or very high frequencies, where the high losses of the passive structures degrade the Q-factor of passive components, and the miniaturization when implemented in monolithic form, as compared to off-chip high-selectivity filters. Active tunable filters also easily compensate for the low-quality factor of tuning elements as varactors. The main disadvantages are the high noise figure, especially when a negative-resistance element is used, and low compression point when small devices and low currents are used. The high noise figure often requires the use of an LNA before the filter in order to make it acceptable.

Among the different types of filters, the best results have been obtained with the cascaded and negative-resistance approaches. Cascaded filters in general have a lower noise figure, but they already include amplifying stages. In fact, the only example of a filter in MMIC technology at a good level of maturity is the tunable cascaded one presented

in [5]. Filters based on active inductors show good potential, but so far have not been developed to a sufficient level of maturity. Filters based on the recursive approach present critical limitations, and do not seem to be viable for practical applications. A comparison table summarizing the better results obtained for each topology is shown in Table 1.

Table 1. Comparison table with the main results obtained for each topology.

Paper	Technology	Frequency (GHz)	Tunability (Relative %)	Bandwidth (Relative %)	Gain (dB)	Noise Figure (dB)	Compression (dBm)
[5]	GaAs HEMT (PH25 UMS)	12	20	10	10	5	−20
[10]	GaAs HEMT (NTT)	1.25	8	2	40	-	-
[12]	Hybrid + GaAs FET ampl.	3.7	6	1	0	17	−5
[21]	GaAs (WIN)	19.5	10	4	0	17	−20
[26]	GaAs (FBH)	1.8	11	6	0	-	−7

It must be remarked again that filters based on GaAs (or, in general, III-V) technologies have been studied in particular in the last 15 years of last century, and have been almost abandoned in this century. With the increase of the operation frequency of the Si- and SiGe-based technologies, the development of active filters at microwave frequencies has started in the last years, with results as potentially interesting as those obtained with N-path filters at lower frequencies.

Author Contributions: Conceptualization, L.P. and G.L.; methodology, L.P., G.L. and F.V.; formal analysis, L.P., G.L. and F.V.; investigation, L.P. and G.L.; resources, F.D. and P.J.; data curation, G.L.; writing—original draft preparation, L.P. and G.L.; writing—review and editing, L.P., G.L.; supervision, F.D. and P.J.; project administration, F.D. and P.J.; funding acquisition, L.P., G.L. and F.V. All authors have read and agreed to the published version of the manuscript.

Funding: This research was funded by ESA, activity ARTES AT 6B.071, grant number: ESA ITT AO/1-10191/20/AB/UK.

Conflicts of Interest: The authors declare no conflict of interest.

References

1. Bonetti, R.R.; Williams, A.E.; Duong, T.; Gupta, R.; Mott, R. An MMIC active filter with 60-dB rejection. In *1992 IEEE MTT-S Microwave Symposium Digest*; IEEE: Albuquerque, NM, USA, 1992; Volume 3, pp. 1195–1198. [CrossRef]
2. Bonetti, R.R.; Williams, A.E. An octave-band MMIC active filter. In Proceedings of the IEEE International Digest on Microwave Symposium, Dallas, TX, USA, 8–10 May 1990; Volume 2, pp. 823–826. [CrossRef]
3. Moazzam, M.R.; Robertson, I.D.; Guglielmi, M. L-band MMIC active filter techniques for future satellite payloads. In Proceedings of the IEEE Colloquium on Recent Advances in Microwave Sub-Systems for Space and Satellite Applications, London, UK, 18 March 1993; pp. 6/1–6/6.
4. Kormanyos, B.K.; Quach, T.K.; Orlando, P.L.; Mattamana, A.G.; Groves, K.S. 26 GHz on chip cascaded filter using low Q inductors. In Proceedings of the 2010 IEEE MTT-S International Microwave Symposium, Anaheim, CA, USA, 23–28 May 2010; p. 1. [CrossRef]
5. Bergeras, F.; Duême, P.; Plaze, J.P.; Darcel, L.; Jarry, B.; Campovecchio, M. Novel MMIC Architectures of wideband microwave active filters for frequency tuning and bandwidth multiplexing. *Microw. Opt. Technol. Lett.* **2011**, *53*. [CrossRef]
6. Kapilevich, B.; Lukjanets, R. High-Q tuned active bandpass filter for wireless application. In Proceedings of the 2000 5th International Conference on Actual Problems of Electronic Instrument Engineering Proceedings, APEIE-2000, Cat, Novosibirsk, Russia, 29 September 2000; Volume 1, pp. 227–230, Devoted to the 50th Anniversary of Novosibirsk State Technical University. [CrossRef]
7. Billonnet, L.; Jarry, B.; Guillon, P. Theoretical and experimental analysis of microwave tunable recursive active filters using power dividers. In Proceedings of the 1993 IEEE MTT-S International Microwave Symposium Digest, Atlanta, GA, USA, 14–18 June 1993; Volume 1, pp. 185–188. [CrossRef]
8. Delmond, M.; Billonnet, L.; Jarry, B.; Guillon, P. High-order monolithic active recursive filter based upon multicellular approach. In Proceedings of the 1996 IEEE MTT-S International Microwave Symposium Digest, San Francisco, CA, USA, 17–21 June 1996; Volume 2, pp. 623–626. [CrossRef]
9. Schindler, M.J.; Tajima, Y. A novel MMIC active filter with lumped and transversal elements. In Proceedings of the Digest of Papers, Microwave and Millimeter-Wave Monolithic Circuits Symposium, Long Beach, CA, USA, 12–13 June 1989; pp. 57–60. [CrossRef]

10. Suwaki, H.; Ohira, T. A very small MMIC variable filter based on a new active filter design concept. In Proceedings of the 12th Annual Symposium on Gallium Arsenide Integrated Circuit (GaAs IC), New Orleans, LA, USA, 7–10 October 1990; pp. 93–96. [CrossRef]
11. Malmqvist, R.; Gustafsson, A.; Alfredsson, M.; Ouacha, A. A tunable active MMIC filter for on-chip X-band radar receiver front-ends. In Proceedings of the 2002 IEEE MTT-S International Microwave Symposium Digest (Cat. No.02CH37278), Seattle, WA, USA, 2–7 June 2002; Volume 3, pp. 1907–1910. [CrossRef]
12. Trabelsi, H.; Cruchon, C. A varactor-tuned active microwave bandpass filter. In *IEEE Microwave and Guided Wave Letters*; IEEE: Piscatway, NJ, USA, 1992; Volume 2, pp. 231–232. [CrossRef]
13. Delmond, M.; Billonnet, L.; Jarry, B.; Guillon, P. Microwave tunable active filter design in MMIC technology using recursive concepts. In Proceedings of the IEEE 1995 Microwave and Millimeter-Wave, Monolithic Circuits Symposium. Digest of Papers, Orlando, FL, USA, 15–16 June 1995; pp. 105–108. [CrossRef]
14. Karacaoglu, U.; Robertson, J.D.; Guglielmi, M. Microstrip bandpass filters with MMIC negative resistance circuits for loss compensation. In Proceedings of the 1994 IEEE MTT-S International Microwave Symposium Digest, San Diego, CA, USA, 23–27 May 1994; pp. 613–616.
15. Karacaoglu, U.; Robertson, I.D. High selectivity varactor-tuned MMIC bandpass filter using lossless active resonators. In Proceedings of the 1994 IEEE MTT-S International Microwave Symposium Digest (Cat. No.94CH3389-4), San Diego, CA, USA, 23–27 May 1994; Volume 2, p. 1191. [CrossRef]
16. Romano, A.; Mansour, R.R. Enhanced-Q microstrip bandpass filter with coupled negative resistors. In Proceedings of the 1997 IEEE MTT-S International Microwave Symposium Digest, Denver, CO, USA, 8–13 June 1997; Volume 2, pp. 709–712. [CrossRef]
17. Garacaoglu, U.; Robertson, I.D. MMIC active bandpass filter using negative resistance elements. In Proceedings of the IEEE 1995 Microwave and Millimeter-Wave, Monolithic Circuits Symposium, Digest of Papers, Orlando, FL, USA, 16–20 May 1995; pp. 171–174. [CrossRef]
18. Huang, K.; Chiang, M.; Tzuang, C.C. A 3.3 mW K-Band 0.18µm 1P6M CMOS Active Bandpass Filter Using Complementary Current-Reuse Pair. In *IEEE Microwave and Wireless Components Letters*; IEEE: Piscatway, NJ, USA, 2008; Volume 18, pp. 94–96. [CrossRef]
19. Ito, M.; Maruhashi, K.; Kishimoto, S.; Ohata, K. 60-GHz-band coplanar MMIC active filters. In *IEEE Transactions on Microwave Theory and Techniques*; IEEE: Piscatway, NJ, USA, 2004; Volume 52, pp. 743–750. [CrossRef]
20. Chang, C.; Itoh, T. Microwave active filters based on coupled negative resistance method. In *IEEE Transactions on Microwave Theory and Techniques*; IEEE: Piscatway, NJ, USA, 1990; Volume 38, pp. 1879–1884. [CrossRef]
21. Chandler, S.R.; Hunter, I.C.; Gardiner, J.G. Active varactor tunable bandpass filter. In *IEEE Microwave and Guided Wave Letters*; IEEE: Piscatway, NJ, USA, 1993; Volume 3, pp. 70–71. [CrossRef]
22. Fan, K.; Weng, C.; Tsai, Z.; Wang, H.; Jeng, S. K-band MMIC active band-pass filters. In *IEEE Microwave and Wireless Components Letters*; IEEE: Piscatway, NJ, USA, 2005; Volume 15, pp. 19–21. [CrossRef]
23. Hsiao, Y.; Meng, C.; Yang, S. 5/60 GHz 0.18 µm CMOS Dual-Mode Dual-Conversion Receiver Using a Tunable Active Filter for 5-GHz Channel Selection. In *IEEE Microwave and Wireless Components Letters*; IEEE: Piscatway, NJ, USA, 2016; Volume 26, pp. 951–953. [CrossRef]
24. Chang, W.L.; Meng, C.; Yang, S.; Huang, G. 0.18 µm SiGe BiCMOS microwave/millimeter-wave dual-mode dual-conversion receiver architecture with a tunable RF channel selection at low-flicker-noise microwave mode. In Proceedings of the 2017 IEEE MTT-S International Microwave Symposium (IMS), Honololu, HI, USA, 4–9 June 2017; p. 1778. [CrossRef]
25. Vindevoghel, J.; Descamps, P. Narrow band active GaAs MMIC filters in K-band. In Proceedings of the 2000 30th European Microwave Conference, Paris, France, 2–5 October 2000; pp. 1–4. [CrossRef]
26. Hopf, B.P.; Wolff, I.; Guglielmi, M. Coplanar MMIC active bandpass filters using negative resistance circuits. In *IEEE Transactions on Microwave Theory and Techniques*; IEEE: Piscatway, NJ, USA, 1994; Volume 42, pp. 2598–2602. [CrossRef]
27. Dardillac, S.; Eyllier, D.; Billonnet, L.; Jarry, B. Active impedance profile technique for selective tuneable active filter with gain. In Proceedings of the IEEE MTT-S International Microwave Symposium Digest, Long Beach, CA, USA, 17 June 2005. [CrossRef]
28. Kaunisto, R.; Alinikula, P.; Stadius, K.; Porra, V. A low-power HBT MMIC filter based on tunable active inductors. In *IEEE Microwave and Guided Wave Letters*; IEEE: Piscatway, NJ, USA, 1997; Volume 7, pp. 209–211. [CrossRef]
29. Xiao, H.; Schaumann, R.; Daasch, W.R.; Wong, P.K.; Pejcinovic, B. A radio-frequency CMOS active inductor and its application in designing high-Q filters. In Proceedings of the 2004 IEEE International Symposium on Circuits and Systems (IEEE Cat. No.04CH37512), Vancouver, BC, Canada, 23–26 May 2004; p. IV-197. [CrossRef]
30. Hsiao, Y.; Meng, C.; Chien, H.C.; Huang, G.W. 2.4-GHz Tunable Miniature CMOS Active Bandpass Filter with Two Transmission Zeros Using Lumped Stepped-Impedance Ring Resonator. In Proceedings of the 2018 IEEE/MTT-S International Microwave Symposium—IMS, Philadelphia, PA, USA, 10–15 June 2018; pp. 405–408. [CrossRef]
31. Pantoli, L.; Stornelli, V.; Leuzzi, G.; Li, H.; Hu, Z. On-chip active filter in GaAs technology for wireless communication systems. *Analog. Integr. Circuits Signal Process.* **2018**, *96*, 1–7. [CrossRef]
32. Pantoli, L.; Stornelli, V.; Leuzzi, G. High dynamic range, low power, tunable, active filter for RF and microwave wireless applications. *IET Microw. Antennas Propag.* **2018**, *12*, 595–601. [CrossRef]

33. Pantoli, L.; Stornelli, V.; Leuzzi, G. Design considerations and effects of class-AB polarization in active filters realized by means of active inductors. In Proceedings of the 2017 47th European Microwave Conference (EuMC), Nuremberg, Germany, 10–12 October 2017; pp. 37–40. [CrossRef]
34. Pantoli, L.; Stornelli, V.; Leuzzi, G.; Hongjun, L.; Zhifu, H. GaAs MMIC tunable active filter. In Proceedings of the 2017 Integrated Nonlinear Microwave and Millimetre-Wave Circuits Workshop (INMMiC), Graz, Austria, 20–21 April 2017; pp. 1–3. [CrossRef]
35. Pantoli, L.; Stornelli, V.; Leuzzi, G. A low-voltage low-power 0.25 μm integrated single transistor active inductor-based filter. *Analog Integr. Circ. Sig. Process* **2016**, *87*, 463. [CrossRef]
36. Pantoli, L.; Stornelli, V.; Leuzzi, G. Low-noise tunable filter design by means of active components. In *Electronics Letters*; Wiley: Hoboken, NJ, USA, 2016; Volume 52, pp. 86–88. [CrossRef]
37. Pantoli, L.; Stornelli, V.; Leuzzi, G. Tunable active filters for RF and microwave applications. *J. Circuits Syst. Comput.* **2014**, *23*, 1450088. [CrossRef]
38. Pantoli, L.; Stornelli, V.; Leuzzi, G. A wideband class-AB tunable active filter. In Proceedings of the 2015 10th European Microwave Integrated Circuits Conference (EuMIC), Paris, France, 7–8 September 2015; pp. 421–424. [CrossRef]
39. Pantoli, L.; Stornelli, V.; Leuzzi, G. Active Filter Synthesis and Optimization Method. In Proceedings of the 7th International Workshop on Microwave Filters, ESTEC—ESA, Noordwijk, The Netherlands, 17–19 April 2018.
40. Pantoli, L.; Stornelli, V.; Leuzzi, G.; Li, H.; Hu, Z. Low-Current Design of GaAs Active Inductor for Active Filters Applications. *Electronics* **2020**, *9*, 1232. [CrossRef]
41. Kaya, A. Design procedure for active microwave filters using the high quality active negative capacitance circuit for RF low-noise bandpass applications. *Microw. Opt. Technol. Lett.* **2008**, *50*, 1086–1093. [CrossRef]
42. Klumperink, E.A.M.; Westerveld, H.J.; Nauta, B. N-path filters and mixer-first receivers: A review. In Proceedings of the 2017 IEEE Custom Integrated Circuits Conference (CICC), Austin, TX, USA, 30 April–3 May 2017; pp. 1–8. [CrossRef]
43. Song, P.; Hashemi, H. RF Filter Synthesis Based on Passively Coupled N-Path Resonators. *IEEE J. Solid-State Circuits* **2019**, *54*, 2475–2486. [CrossRef]
44. Luo, C.-k.; Gudem, P.S.; Buckwalter, J.F. A 0.4–6-GHz 17-dBm B1dB 36-dBm IIP3 Channel-Selecting Low-Noise Amplifier for SAW-Less 3G/4G FDD Diversity Receivers. *IEEE Trans. Microw. Theory Tech.* **2016**, *64*, 1110–1121. [CrossRef]
45. Kibaroglu, K.; Rebeiz, G.M. An N-path bandpass filter with a tuning range of 0.1–12 GHz and stopband rejection > 20 dB in 32 nm SOI CMOS. In In Proceedings of the 2016 IEEE MTT-S International Microwave Symposium (IMS), San Francisco, CA, USA, 22–27 May 2016; pp. 1–3. [CrossRef]